Since January 2020 Elsevier has created a COVID-19 resource centre with free information in English and Mandarin on the novel coronavirus COVID-19. The COVID-19 resource centre is hosted on Elsevier Connect, the company's public news and information website.

Planetary and Space Science 194 (2020) 105105

Contents lists available at ScienceDirect

Planetary and Space Science

journal homepage: www.elsevier.com/locate/pss

Review Article

Erosion of lunar surface rocks by impact processes: A synthesis

Friedrich Hörz [a,*], Alexander T. Basilevsky [b], James W. Head [c], Mark J. Cintala [d]

[a] Jacobs-JETS, 2224 Bay Area Boulevard, Houston, TX, 77058, USA
[b] Vernadsky Institute of Geochemistry and Analytical Chemistry, Russian Academy of Sciences, Moscow, 1199991, Russia
[c] Department of Geological Sciences, Brown University, Providence, RI, 02912, USA
[d] Code XI3, NASA Johnson Space Center, 2101 NASA Parkway, Houston, TX, 77058, USA

ARTICLE INFO

Keywords:
Planetary regoliths
Crater-morphology
Thermal fatigue
Particle abrasion
Collisional fragmentation
Rock erosion

ABSTRACT

This report summarizes observations of returned Apollo rocks and soils, lunar surface images, orbital observations, and experimental impacts related to the erosion and comminution of rocks exposed at the lunar surface. The objective is to develop rigorous criteria for the recognition of impact processes that assist in distinguishing "impact" from other potential erosional processes, particularly thermal fatigue, which has recently been advocated specifically for asteroids. Impact in rock is a process that is centrally to bilaterally symmetric, resulting in highly crushed, high-albedo, quasicircular depressions surrounded by volumetrically prominent spall zones. Containing central glass-lined pits in many cases, such features provide distinctive evidence of impact that is not duplicated by any other process. Additional evidence of impact can include radial fracture systems in the target that emanate from the impact point and clusters of fragments that attest to the lateral acceleration and displacement of each one. It is also important to note that impact produces a wide variety of fragment shapes that might totally overlap with those produced by thermal fatigue; we consider fragment shape to be an unreliable criterion for either process. The stochastic nature of the impact process will result in exponential survival times of surface rocks; that is, rock destruction initially is relatively efficient, but it is followed by ever increasing surface times for the last rock remnants. Thermal fatigue, however, is essentially a thermal-equilibrium process. The corresponding distribution of survival times should be much more peaked in comparison, presumably Gaussian, and diagnostically different from that due to impact. Given the abundance of evidence that has been gleaned from *returned* Apollo rocks and soils, it is surprising how little has been learned about the impact process from the *photography* of rocks and boulders taken by the astronauts on the lunar surface. This suggests that it will require rocks and soils returned from asteroids to evaluate the relative roles of thermal versus impact-triggered rock erosion, particularly when both processes are likely to be operating.

1. Introduction

An unconsolidated, global surface deposit of debris typically a few meters thick, the lunar regolith is the result of impact-cratering processes that extend over scales from sub-micrometers to kilometers (*e. g.*, McKay et al., 1991; Costello et al., 2018). Summarizing a wide variety of experimental-impact studies, lunar-surface observations, and statistical modeling efforts, Quaide and Oberbeck (1975) describe the macroscopic growth of this debris layer by the in-situ comminution of bedrock, along with its vertical and lateral displacement and transport in the form of crater ejecta. With increasing regolith thickness, the system becomes self-buffering, as larger and larger craters are required to reach and excavate bedrock, thereby adding new material to the growing deposit (*e.g.*, Hartmann, 1985). The size-frequency distribution of these craters has a cumulative slope of log −2.5 to −4 (Neukum et al., 1973; Hörz et al., 1991; Speyerer et al., 2016; Pokorny et al., 2019), indicating that small-scale impacts are much more frequent than larger events. The much more active, small-scale regime erodes and modifies the relatively blocky bedrock ejecta such that fine-grained materials totally dominate the mechanical, petrographic, and compositional characteristics of the evolving "soils." The regolith "matures" over time, such that many of its characteristics (*e.g.*, grain-size distribution and modal make-up) bear little resemblance to freshly excavated crater ejecta (*e.g.*, Papike et al., 1981, 1982; McKay et al., 1991; Hörz and Cintala, 1997).

An important aspect of this regolith-maturation process is the additional, in-situ comminution of comparatively coarse, fresh, bedrock

* Corresponding author.
E-mail address: friedrich.p.horz@nasa.gov (F. Hörz).

https://doi.org/10.1016/j.pss.2020.105105
Received 29 May 2020; Received in revised form 11 September 2020; Accepted 18 September 2020
Available online 25 September 2020
0032-0633/

ejecta that are deposited at the surface and thus exposed to incessant bombardment by small-scale impacts. The mass of an exposed rock relative to the energy of each individual impact is the principle factor in determining how erosion will proceed. Small impacts will cause abrasion through a cosmic, high-speed version of sandblasting, (*e.g.*, Hörz et al., 1974), while sufficiently energetic impacts could rupture or even pulverize the rock (Gault and Wedekind, 1969; Fujiwara et al., 1989; Housen and Holsapple, 1999; Cintala and Hörz, 2008). Monte Carlo-based, statistical modeling of these erosional processes yielded the "survival times" of hand-specimen-sized lunar rocks at a variety of probability levels (Hörz et al., 1975). These model times were recently revised and improved by counting the frequency of surface rocks >2 m in size around craters of known formation age as derived from measurements of cosmic-ray exposure times on Apollo samples (Basilevsky et al., 2013, 2015). They found that approximately 50% of all surface boulders >1 m diameter had disappeared after about 40–50 Ma, yet a few such boulders survived for as long as 200–300 Ma. Additionally, Gent et al. (2014, 2016) deduced the frequency of boulders >1 m in the continuous ejecta deposits surrounding large craters (~10–30 km in diameter) using the Diviner thermal radiometer and radar instruments onboard the Lunar Reconnaissance Orbiter (LRO). They observed that all meter-sized surface blocks were essentially destroyed after about 1 Ga. As did that of Basilevsky et al., the work of Gent et al. also establishes that the number of meter-sized boulders decreases as the morphological degradation of the parent crater increases, which occurs over time scales measured in hundreds of millions of years for structures of this size. Thus, statistical modeling of the impact process and lunar observations combine into the view that boulders on the lunar surface erode rather efficiently within relatively short times after emplacement, yet a small fraction of such rocks will also survive for very long times. This nonlinear survival behavior is the inescapable result of the stochastic nature of the bombardment process.

It has been suggested that thermal cycling provides an additional erosion process on the surfaces of planetary bodies without atmospheres, including the Moon (Molaro and Byrne, 2012; Delbo et al., 2014; Molaro et al., 2017). This view appeared to be corroborated by the images obtained from the OSIRIS-REx mission to asteroid Bennu and the Hayabusa 2 mission to asteroid Ryugu (Molaro et al., 2019a,b; Lauretta et al., 2019).

Impact and thermal-fatigue processes should occur concurrently, and their effects should be manifested in returned lunar samples that can be investigated at scales ranging from decimeters to sub-micrometers. The two processes might produce some similar features, but they should also differ in ways that are consistent with their modes of energy deposition, amplitudes of stress, and rates of deformation, which differ between the two processes by many orders of magnitude. It is paramount, therefore, to develop criteria that could be diagnostic of each process, with the ultimate goal of understanding the relative roles of both processes in the destruction of surface rocks and the development of lunar and asteroidal regoliths.

Our goal in the present paper is to summarize the impact process, primarily by examining the surfaces of returned Apollo rocks. The general approach is based entirely on visual examples and characteristics of the collisional process from micrometer to decimeter scales. Thus, we examine that energy regime which dominates the comminution of fresh, relatively coarse, bedrock ejecta. Where possible, we complement the lunar observations with experimental analogs, which form the basis for a more quantitative understanding of the impact process.

We first introduce the size-dependent morphologies of typical craters in dense rock, which differ dramatically from the bowl-shaped structures in unconsolidated targets. We then proceed to typical features of lunar rocks that illustrate erosion via small-scale, sandblasting effects as well as catastrophic, collisional-fragmentation processes. We conclude with statistical models of lunar-rock erosion, lunar-surface observations into the survival times of meter-sized boulders, and the impact-generated nature of the fine-grained regolith matrix. The insights gained from these investigations should be helpful in distinguishing between impact processes and erosion induced by thermal stress.

2. Crater morphology

Hypervelocity craters on returned lunar rocks and soil grains are usually referred to as "microcraters," and their morphologies indicate targets of considerable cohesion, *i.e.*, dense rocks. Microcraters are characterized by three morphological features (Hörz et al., 1971a, 1971b; Hartung et al., 1972a, 1972b; Schneider et al., 1973): a deep, central pit; a concentric halo zone in the immediate vicinity of the pit; and a relatively large, concentric spall zone. The diameter of the halo (D_h) is typically 1.2 to 2.5 the diameter of the central pit (D_p), while the diameter of the spall zone (D_s) is 4–7 D_p. The pit is, by definition, a deep, cup-shaped, glass-lined depression and it is typically such a striking feature that microcraters are frequently referred to as "pit craters" or, for short, "zap pits." The "halo" represents highly shocked, finely crushed material of high albedo that surrounds the pit as a concentric shell; it is also present under the pit.

As we will demonstrate below, the significance of these three morphologic features varies with size of the crater (Hartung et al., 1972a, 1972b; McDonnell et al., 1972; Hörz et al., 1991): small craters (<1 μm) are characterized by a central pit only, while craters >10 cm often can be detected only as a relatively shallow spall zone. The change from pit-only to spall-only morphologies is gradual, with many intermediate examples characterizing the crater populations in the millimeter-to-centimeter size range. While most of these crater features are remarkably centrosymmetric, deviations from this are not uncommon, depending on the nature of the specific target site: elongate microcraters may form at the contact of two different minerals, for example, which have different physical properties, or in a single feldspar grain with pronounced cleavage. Also, the detailed surface relief of the target site on the scale of the evolving crater greatly affects the circularity of the pit and especially the spall zone.

As documented by many during the early Apollo program (Hörz et al., 1971a, 1971b; Morrison et al., 1972; McDonnell et al., 1972; Hartung et al., 1972a; Neukum et al., 1973; and others), the progressive changes in crater morphology are best illustrated on glass surfaces, either in the form of solid spheres or splashes of quenched impact melt that occasionally drape lunar rocks (*e.g.*, See et al., 1986). Such glass surfaces constitute targets that are more homogeneous in their physical properties than crystalline rocks, and being relatively smooth, they have little surface relief, thus better preserving the centrosymmetric nature of the shock wave and the resulting impact features. Fig. 1 illustrates representative "small" (<100 μm) craters on glass surfaces.

The smallest craters (<1 μm) are manifested only as relatively deep pits, with typical depth/diameter values > 0.5 (Fig. 1A). These submicrometer craters are also characterized by relatively tall and narrow "lips" (Hartung et al., 1972a, 1972b), which develop into relatively broad rims as crater size increases from 1 to 5 μm (Fig. 1 B). The interiors of these pit-only craters are lined with impact melt and the raised lips and broad rims seem to be a combination of plastically deformed target and impact melt that quenched and froze as it flowed out of the crater. As crater size increases (5–10 μm; Hartung et al., 1972a, 1972b), the first signs of incipient spallation become visible in the form of short arcs (Fig. 1 C and D) that eventually combine into a continuous, concentric fracture system and a fully developed spall zone (Fig. 1E). At sizes above 100 μm, many craters are characterized by a spall zone only. Fig. 1E and F illustrate examples with and without central pits to illustrate that the material immediately below the central pit is highly crushed and presumably very weak, in stark contrast to the glass-lined pit.

Also, the spallation process undercuts the pit, making it more prone to removal, a process that seems to require little energy (Hörz et al., 1971a, 1971b). Removal of the pit might have been part of the actual cratering event or it might have happened at some later time, either by shocks from neighboring impacts or during general regolith "gardening" and related

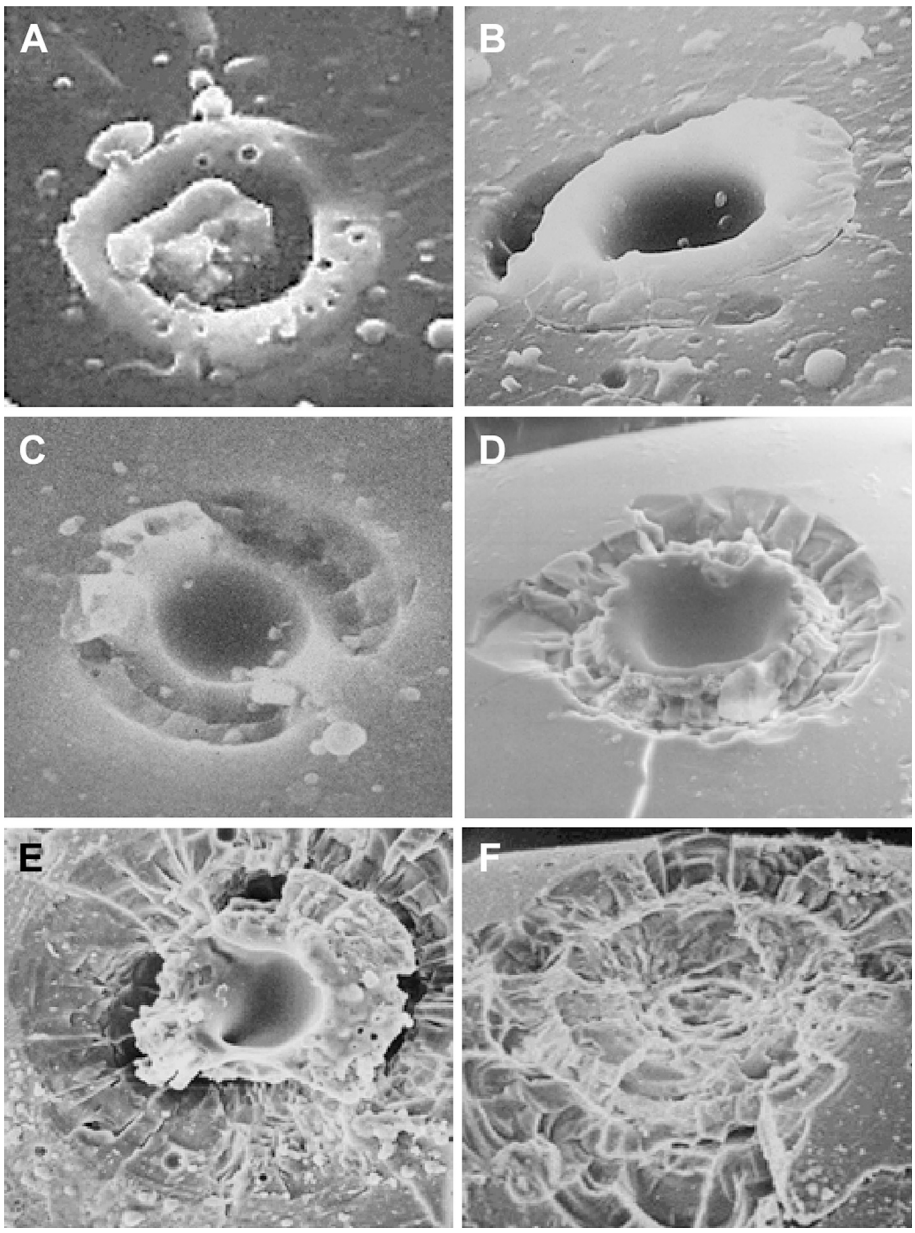

Fig. 1. Typical lunar microcraters on glass surfaces, illustrating the change in crater morphology with increasing crater size. (A) Crater diameter = 3 μm, (B) 6 μm, (C) 14 μm, (D) 55 μm, (E) 220 μm, and(F) 250 μm. Please see the text for details. (Images (A), (B), (E), and (F) from Hartung et al., 1972a); (C) and (D) from D.S. McKay, unpublished).

tumbling of the host rock. As a consequence, we postulate that the majority of "spall-only" craters on lunar rocks initially contained a glass-lined pit, and that spall-only craters on lunar rocks are also the products of high-velocity impact. This seems especially likely if the center of a spall crater consists of intensely crushed materials of high albedo.

In summary, all craters on glass targets <1 μm in diameter are of the "pit-only" type and all structures >10 μm have fully developed spall zones with transitional stages occurring over the 1–10 μm size range. Many craters >50 μm might have lost their glass-lined pits, yet all have highly crushed centers which are typically of high albedo.

Unfortunately, electron-microscope methods have not yet been used in morphologic studies of craters in the 1-1000-μm size range on crystalline rocks. The glass surfaces are simply much more suitable for the study of craters in this size range. Deducing crater-production rates and associated fluxes of small-scale impactors also meets with fewer complications when using homogeneous glass. The most detailed morphologic studies of millimeter-to centimeter-sized craters on breccias and crystalline rocks are those by Hörz et al. (1971a, 1971b), Morrison et al. (1972), and Neukum et al. (1973). The following is a brief summary.

Fig. 2A illustrates a cm-sized event and numerous small craters on lunar rock 68416, a crystallized, fine-grained impact melt rock; note the relatively large spall zone compared to the central, dark, glass-lined pit. Fig. 2B shows a similar sample (rock 73216) with a rather similar population of microcraters. All small, dark spots in Fig. 2A and B are glass-lined pits; the glass is dark because it contains iron from either olivine or pyroxene that resided in the melt zone of each crater. Occasionally, pits are confined to iron-free, single-crystal feldspars and have, therefore, rather transparent melt linings. Importantly and as illustrated in Fig. 2A and B, all pits are surrounded by haloes of highly crushed and thus high-albedo material. Many high-albedo spots exist in these images, each of which reflects the center of an impact feature whose central pit has been removed. Also note that only the youngest of these craters have clearly

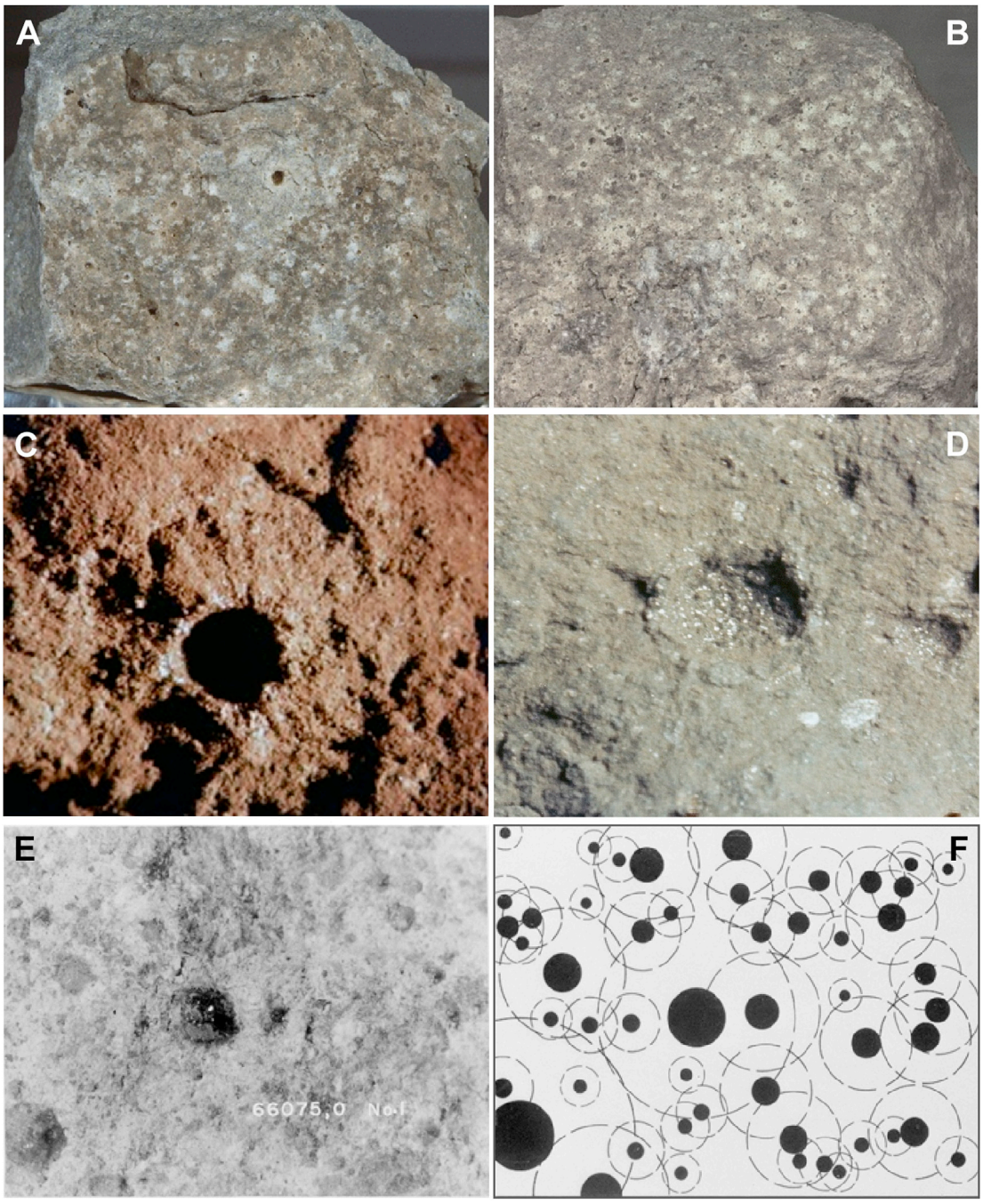

Fig. 2. Relatively large, millimeter-sized craters and their spall zones on lunar rocks. (A) Lunar rock 68416 (8 cm long, 178 g) displays a large pit that is surrounded by a spall zone of modestly elevated albedo. Note the presence of a much brighter halo surrounding this and every other glass-lined pit, which can be recognized as dark spots [NASA photograph S72-37535]. (B) Lunar rock 73216 (7 cm long, 162 g) displaying a similar population of microcraters, each of which either retains a dark pit or is visible as a finely crushed, high-albedo center [NASA photograph S73-16778]. (C) and (D) illustrate closeups of millimeter-sized, glass-lined, pit craters on breccia surfaces, with the grazing illumination in (C) enhancing visibility of the spall zone [C, Hörz et al., 1971a, 1971b; D, Hörz, unpublished]. (E) Cratered breccia surface (rock 66075, 10 cm long, 347 g); the FOV is some 2 cm across [NASA photograph S72-48967]. (F) Reconstruction of initial spall zones around each pit crater recognized in (E) (from Neukum et al., 1973). For additional details see text. Note that all images of Apollo rocks throughout this report (and many additional ones) may be found in the Lunar Sample Compendium (https://curator.jsc.nasa.gov/lunar/lsc/).

discernible spall zones; most of them do not, yet the trained eye can discern spall zones around some 20–30% of all craters in crystalline rocks.

Fig. 2C illustrates a fresh crater formed in a friable regolith breccia while Fig. 2D shows a modestly eroded crater with a barely discernible spall zone in another breccia. Both examples show that the spall zones in porous, physically heterogeneous breccias are smaller (typically, D_s = 3–5 D_P) than those in dense glass and crystalline rocks (D_s = 4–7 D_p). Interestingly, the glass-lined pits in modestly coherent, fine-grained breccias are more often retained than in crystalline rocks, as they appear to be welded to the fine-grained breccia matrix. That, in turn, is less crushed and fractured in the immediate surroundings of the pit than it is in the crystalline rocks. The smaller spall zones and better retention of the pits both appear to be related to the less efficient propagation or, equivalently, more rapid attenuation of the shock through a porous, and thus physically heterogeneous, medium (*e.g.*, Kieffer, 1971; Melosh,

1989). Fig. 2E shows a typical, densely cratered breccia surface; Fig. 2F associates each pit of Fig. 2E with a spall zone of $D_s = 4\ D_p$ to illustrate the common overlap of many impact events, most of them having lost their spall zone(s) to erosion. There is no doubt that friable breccias display pit densities (number/cm^2) much higher than those on crystalline rocks (Neukum et al., 1973). It is not a recommended practice to derive an exposure age of a sample from measurements of crater densities without accounting for the physical properties of the host rock (Neukum et al., 1973).

In Summary, Fig. 2 provides evidence that a dark melt pit surrounded by a light-colored halo are the tell-tale features of millimeter-sized craters on crystalline, feldspar bearing, lunar rock surfaces. The central pit is dislodged in many cases, however, and the high-albedo halo, typically residing in a modest, local depression, is the only remaining evidence for hypervelocity impact. Spall zones appear to be especially short-lived and prone to erosion, as they are low-relief features even when fresh; many spall zones are manifested only by partial arcs around many millimeter-sized craters. Craters on poorly consolidated breccias derived from the local regolith have glass-lined pits that are somewhat deeper than their crystalline equivalents, consistent with greater penetration depth in a lower-density medium. The radial extents of their spall zones are somewhat less than the crystalline equivalents, again consistent with the more rapid shock decay in the porous breccias. Smaller spall zones result in less destruction of neighboring craters, which is why crater densities are somewhat higher on modestly coherent regolith breccias than on competent rocks. All in all, however, these differences are subtle and the basic crater morphologies for millimeter-to centimeter-size craters described for glasses and crystalline rocks also apply to breccias.

Of course, craters much larger than centimeters, especially those greater than decimeters, cannot be sustained and observed on the relatively small, typically <1 kg, lunar rocks returned by Apollo. One of the largest craters on all returned rocks, 3.5 cm in maximum spall diameter, is illustrated in Fig. 3A; its spall zone is asymmetric due to the local surface relief and associated removal of local promontories. The morphology of still larger, decimeter-sized craters must be deduced from lunar-surface imagery of relatively large boulders. Some 20 m^2 of boulder surfaces were examined extensively in images from Apollos 14 through 17, and not a single "classic" crater – consisting of a central pit, surrounding halo, and spall zone – was found; neither were any isolated pits (Hörz, unpublished). A well-developed spall zone from Outhouse Rock of Apollo 16 (Fig. 3B) is the only unambiguous impact structure observed on any image of all Apollo boulders. It was photographed and sampled only because astronauts Young and Duke recognized it for what it was. No other Apollo crew observed or photographed a similar structure. Note that this Apollo 16 spall feature contains a severely crushed halo in its center, as is found in its much smaller counterparts, which is the reason it is deemed a hypervelocity feature. Distinct arcs, and thus parts of spall zones (see Fig. 3C), can be observed, however, in some boulder photos,

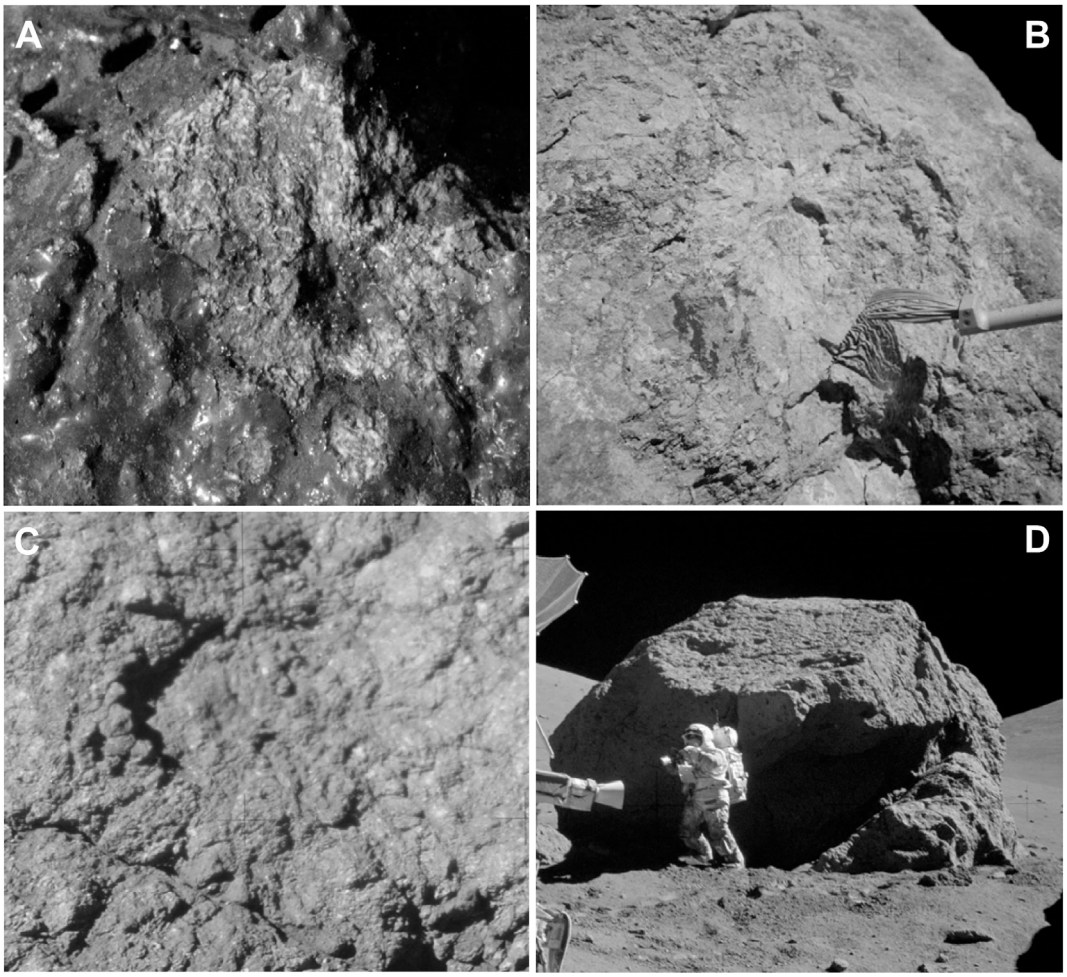

Fig. 3. "Large" craters on lunar rocks and boulders. (A) Pit crater and surrounding spall zone, some 3 cm in diameter, on a glass-draped Apollo 12 rock (12054, 9 cm long, 687 kg). (B) Large spall zone, at least 50 cm across, on Apollo 16 "Outhouse" rock. This is the largest, unambiguous impact feature on all Apollo boulders; note the crushed material in its center [NASA photograph AS16-106-17345]. (C) Another, partly preserved spall zone (some 30 cm in diameter) on an Apollo 17 (Station 6) breccia boulder [NASA photograph AS17-146-22307]. (D) Circular impact feature on the top surface of an exceptionally large Apollo 17 (Station 6) boulder; note the large fragment at the lower-right edge of the block that was dislodged from this boulder [NASA photograph AS17-146-22294]. Please see the text for details.

especially in stereo images. A circular depression suggesting impact is also seen on a massive Apollo 17 boulder as illustrated in Fig. 3D. This possible impact is in an ideal location to have spalled off the large fragment near and partly under the boulder's overhang. A number of partly preserved spalls and halo patches appear to be present on additional boulders, yet most of them are seen only by the trained eye familiar with the fresh and degraded populations of millimeter-sized craters on returned rocks.

There can be no doubt that large boulders (>1 m) will suffer impacts that produce decimeter-sized craters, given the size-distribution and the frequency of prospective impactors (Neukum et al., 1973; Fechtig et al., 1974; Grün et al., 1985; Love and Brownlee, 1993; Hiesinger et al., 2012; Speyerer et al., 2016). Since we never observed a single, large, central pit on any boulder (Hörz, unpublished) we conclude that decimeter-sized craters will systematically shed their central pits as part of the actual cratering process. The pristine morphology of "large" craters would then be manifested only as a central halo patch and a relatively shallow spall zone. Given the rarity of decimeter-size events compared to the numerous, much smaller impacts, the pristine spall zone will be eroded beyond recognition rather rapidly and on timescales that are short compared to the production rate of decimeter-sized craters. As a consequence, only exceptionally recent events will remain recognizable.

The apparent lack of recognizable cratering events on lunar boulders points towards the limitations of planetary surface images versus the potential of returned samples. Little would be known about the small-scale bombardment history and associated effects from the surface photography of Apollo alone, yet every returned surface, from rocks to tiny soil grains exposed to space, displays unambiguous signs of impact. This could be due, in part, to the spatial resolution of the images and the lack of true, close-up boulder photography from Apollo. It is probably related more, however, to the production of shallow spall zones and their relatively rapid degradation when crater diameters attain decimeter scales and larger.

Importantly, major morphologic features of microcraters can be reproduced in the laboratory as shown in Fig. 4. Sub-micrometer-size craters, produced with electrostatic particle accelerators at around 10

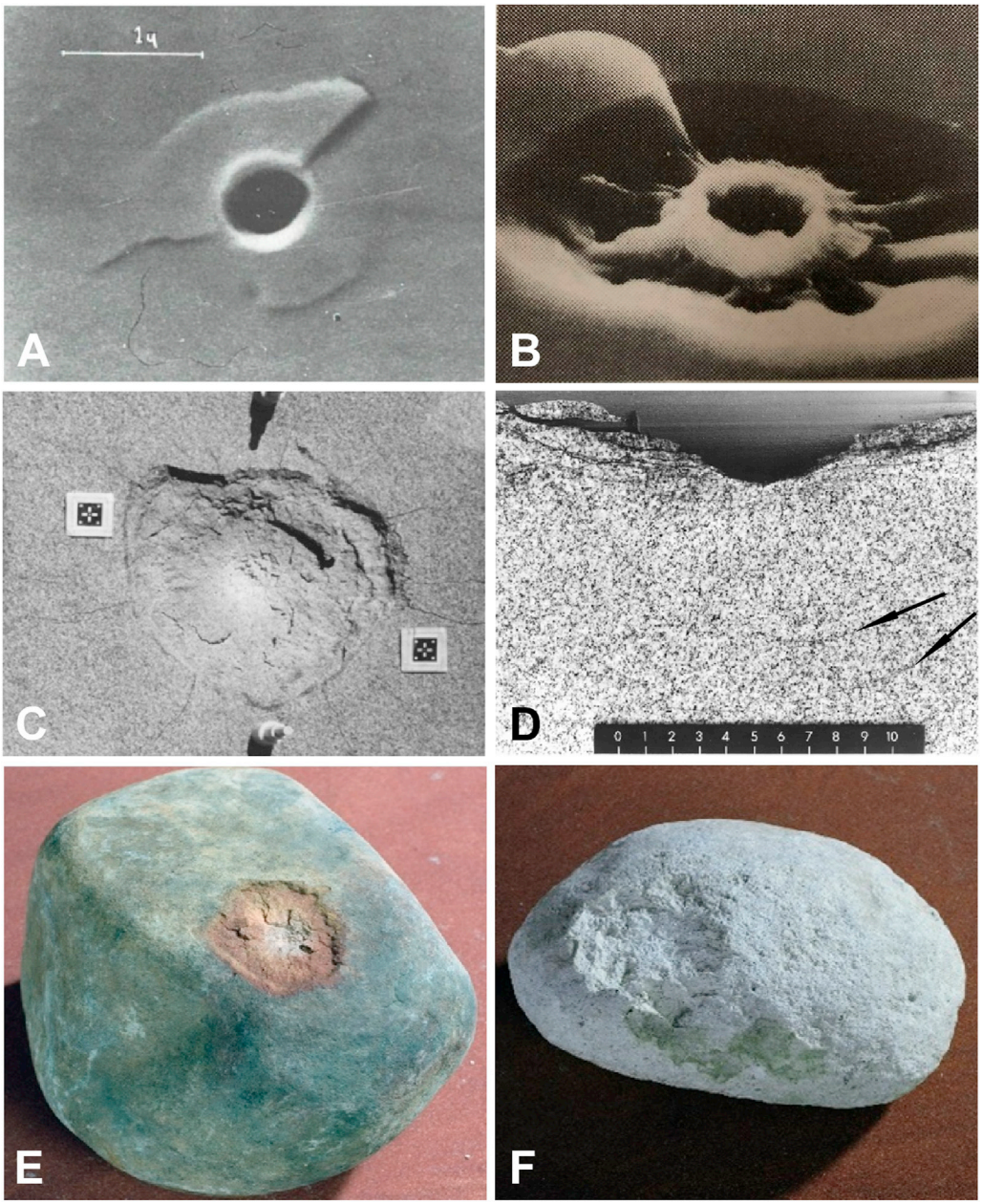

Fig. 4. Examples of experimental hypervelocity craters of various sizes. (A) Micron-size crater produced by an iron projectile into a polished quartz-glass target at 7 km s^{-1} (McDonnell et al., 1972). (B) Microcrater with a spall zone 25 μm in diameter (aluminum projectile at 5 km s^{-1} into quartz glass; Neukum et al., 1972). (C) 26 cm (average) diameter crater in a granite target produced by 12.7-cm aluminum sphere impacting at 7.3 km s^{-1} (Hörz, 1969). (D) Close-up of the cross-sectioned crater cavity of (C), illustrating two prominent fracture systems: a shallow, near surface one that produces the spall zone and a concentric set (black arrows) that disrupts the target at depth. (E) 6-cm crater in a sandstone river rock (3-mm glass projectile at 5.5 km s^{-1}). (F) 8-cm crater in a limestone boulder (3-mm glass sphere at 5.6 km s^{-1}). See text for additional details. The experiments in (E) and (F) were conducted in JSC's Experimental Impact Laboratory (EIL) and are unpublished.

km s^{-1}, are also "pit-only" structures, and as crater size increases, one observes incipient as well as complete spallation (Fig. 4A and B). These accelerators, however, are limited to projectiles <50 μm in size and are not suitable for creating millimeter-scale or larger craters. Larger events dictate the use of light-gas guns, which can employ larger projectiles but are inherently limited to speeds around 7 km s^{-1}. Despite numerous light-gas gun cratering experiments from millimeter to decimeter scales in dense rocks or glasses, not a single one could produce a central pit. Instead, all light-gas gun experiments resulted only in relatively shallow depressions, totally controlled by spallation processes. As illustrated in a granite target in Fig. 4C, all of these depressions still have in their centers highly crushed material of higher albedo than the surrounding host rock. Note the 7 km s^{-1} of that granite impact produced a shock stress of some 80 GPa, which should be sufficient to melt granite, yet there was no central pit in this crater (Fig. 4C or D). We do not know whether a pit was produced in this light-gas gun experiment, only to be displaced and destroyed as part of the cratering process, but we suspect that the formation of glass-lined pits requires speeds much higher than 7 km s^{-1}. Hörz (1969) carefully collected and investigated the ejecta of this granite crater and did not find any melt, much less the remnants of a melt-lined pit which one observes, albeit rarely, in lunar soils. Also, the cursory observation of ejecta from numerous other experimental craters in rock has never yielded any such pit shards. It is thus possible that the velocity regime accessible to light-gas guns is insufficient to make glass-lined pits. On the other hand, it appears that even higher, natural impact speeds produce a spall zone only, once crater diameter exceeds about 10 cm.

To summarize this section of detailed crater morphology, we observe that the ideal and unambiguous crater in dense rocks is characterized by a glass-lined central pit that is surrounded by a concentric zone of crushed, high-albedo material, with both residing within a much larger concentric zone of prominent, but shallow, spallation. The radius of the high-albedo material is typically twice the diameter of the pit, with the spall zone 3–7 times the pit diameter, depending on the cohesion of the target rock and the rock's local surface relief. Both the pit and the halo reside in the center of a local depression created by the spall. Submicron craters are of the pit-only type, while decimeter-sized craters contain no pits and manifest themselves only as relatively shallow spall zones with crushed, high-albedo material in the center. Depending on the physical heterogeneity of the target site and its topographic relief, individual craters can deviate substantially from the ideally centrosymmetric plan view.

Ballouz et al. (2020) summarize the crater structures that are observed on the surfaces of boulders on asteroid Bennu at image resolutions as high as 1 cm/pixel, approximately comparable to the Apollo surface photography, yet greatly inferior to laboratory observations of returned rocks. Their Fig. 1 shows decimeter-size depressions that could indeed represent spall zones that are so typical of impacts into competent rock. Many of these candidate structures, however, are sufficiently pixelated that their detailed morphologies, and thus origins, are difficult to ascertain.

3. Rock erosion by abrasion

Impact is a stochastic process, and the size, spatial distribution and formation times of the regolith-forming craters are random. Given the steep, cumulative size-distribution of craters and associated impactors (Neukum et al., 1973; Fechtig et al., 1974; Hörz et al., 1991; Speyerer et al., 2016, and others), any rock residing at the lunar surface will be bombarded incessantly by very small projectiles, each removing a tiny fraction of the rock's mass. One may view this small-scale cratering regime as equivalent to sandblasting at unusually high particle speeds. The net effect is the gradual abrasion of rocks exposed at the surface. Given the stochastic nature of the impact process, however, there is also the finite probability that a target rock will be ruptured, if not completely fragmented, by a sufficiently energetic projectile. As a consequence, we recognize two, very distinct, erosive regimes: *impact-induced abrasion* and *catastrophic fragmentation* of lunar rocks. The regime into which a specific impact would be classified is strongly dependent on the absolute mass of the target rock: what could be a single, fatal blow to a 100-g rock would just be part of the abrasive regime for a multiple-ton boulder. We will deal with the abrasion process first, to be followed by a separate section on collisional fragmentation.

Fig. 5 illustrates effects of the abrasion process, once again best demonstrated on glass surfaces. Fig. 5A shows a glass sphere of quenched impact melt, 450 μm across, and impact craters of various sizes; two large craters (one in side view) dominate this glass bead, yet smaller craters are present as well. Fig. 5B shows a 3-cm glass sphere with a population of relatively small craters, each removing a tiny fraction of the mass of the sphere. On the other hand, a substantial, nearly catastrophic event dislodged almost half of the entire sphere. Fig. 5C represents a large (6 cm) glass splash that draped a crystalline rock fragment. This sample was obviously exposed to space for a much longer period than the sphere of Fig. 5B, thus acquiring a much higher crater density and many larger craters. Again, a very energetic event might have catastrophically removed a large fraction of the glass and part of the crystalline core. Note also, that the "exposed" ridge of Fig. 5C ellipsoid has higher crater densities than the sides, consistent with its exposure geometry to an isotropic particle flux. The antipodal surface is uncratered and was not exposed to space. Fig. 5D illustrates a well-rounded crystalline rock, typical of many. Obviously, all rounded and abraded surfaces must have been exposed to space for a long time and they acquired crater densities much higher than those illustrated on the glass surfaces of Fig. 5A–C. Indeed, the crater populations of rounded rocks are typically in "equilibrium," which implies that every new event will statistically destroy an existing one, identical to the evolution of large scale-crater populations (*e.g.*, Hiesinger et al., 2012; Minton et al., 2019). Most Apollo rocks resided on the lunar surface long enough to acquire equilibrium crater populations. Production populations, as shown in Fig. 5A–C, are rare and observed on < 10% of all returned, hand-specimen-sized (>100g) rocks.

Fig. 5E illustrates lunar rock 14310, a 3.5 kg, fully crystallized impact melt and the most outstanding example among all Apollo samples of the effects of impact-induced surface abrasion and rounding. Note the heavily cratered, rounded and abraded surfaces that were exposed, which contrast markedly with the jagged fracture surfaces of the buried, totally uncratered portion. Most lunar rocks are cratered on all sides, attesting that they tumbled repeatedly at the lunar surface; simple, one-step exposure histories as reflected by rock 14310 are rare, comprising <10% of all rocks collected (Hörz et al., 1972 and unpublished estimate).

The different components making up breccias, such as matrix and diverse clasts, have different physical properties that result in idiosyncratic erosion rates for each component, with the less-consolidated matrix generally being removed more easily, and competent clasts forming topographic highs, if not promontories. At the Apollo 16 site is House Rock (Fig. 5F), which is some 12 m tall, 16 m wide and 20 m long. It displays the typical erosional, knobby, relief of large breccia boulders and, as a block of ejecta from North Ray Crater (Ulrich et al., 1981), reflects erosion over the last 50 million years. Note that the "abrasive" regime on this large boulder includes projectiles much more energetic than those that shaped the erosional surfaces of any of the other rocks shown in Fig. 5, yet the surfaces of the large boulder are still relatively smooth and the boulder is somewhat rounded overall. Impact-induced abrasion thus occurs over a wide range of target masses, from individual regolith grains to the largest blocks of ejecta.

4. Rock erosion by collisional fragmentation

As discussed above, there is a finite probability that any surface rock might suffer an impact sufficiently energetic to fragment and thus destroy it. The process of collisional fragmentation has been extensively studied experimentally (*e.g.*, Gault and Wedekind, 1969; Fujiwara et al., 1989; Davis and Ryan, 1990; Ryan et al., 1991; Housen and Holsapple, 1999; Flynn and Durda, 2004; Cintala and Hörz, 2008; among many others), as

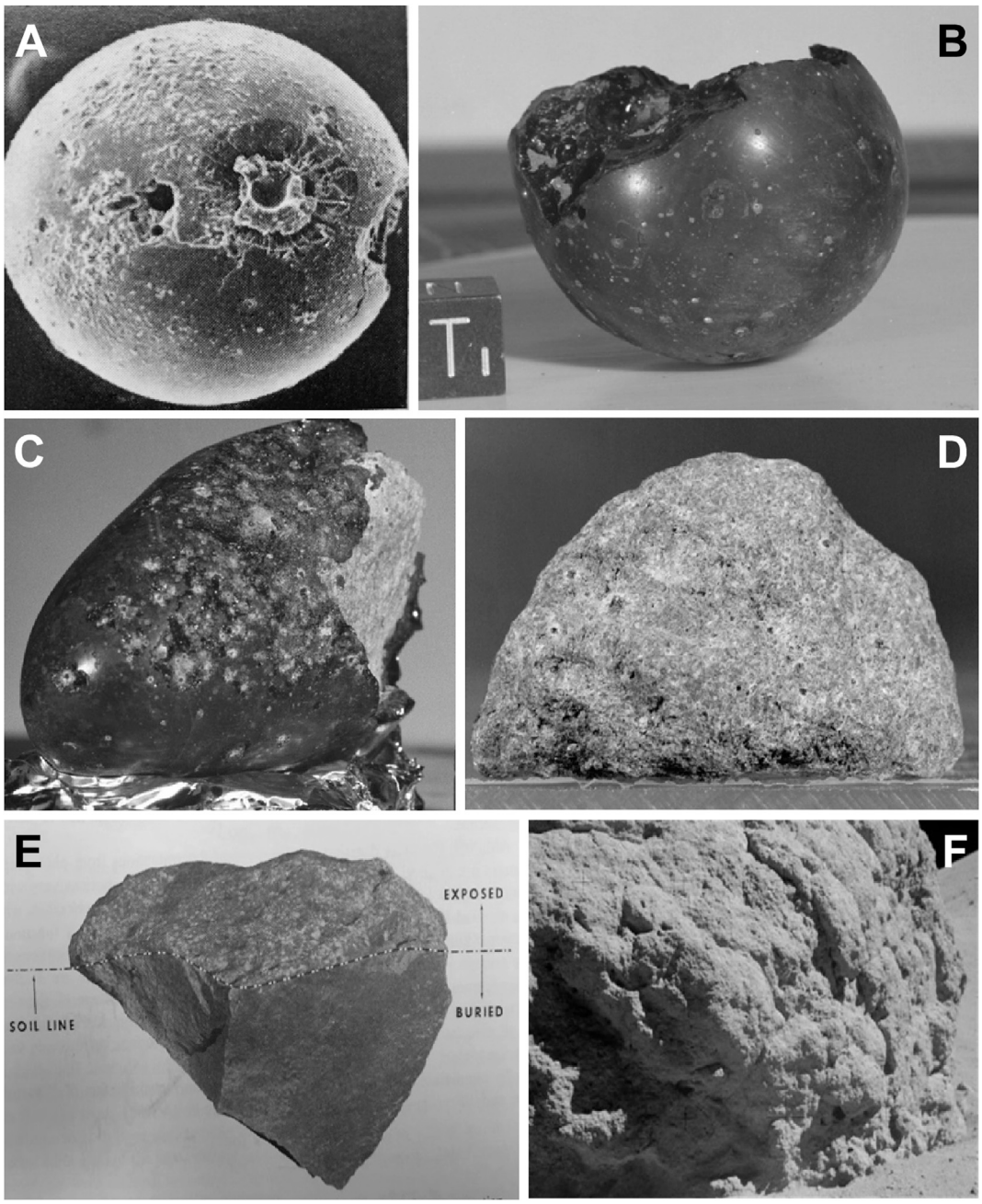

Fig. 5. Examples of lunar rock erosion by impact-induced abrasion. (A) Small glass sphere (450 μm in diameter) illustrating two "large" craters as well as smaller structures (Hartung et al., 1972a). (B) Lunar sample 60095, a glass sphere (about 3.5 cm in diameter and weighing 57 g) that has been pitted by just a few, relatively small microcraters. The orientation cube in this image (and others to follow) is 1 cm on a side. (C) Lunar rock 64455 (5 cm long, 57 g) is a glassy melt splash that draped a crystalline host. (D) Lunar rock 12017 (about 5 cm long, 57g) is well rounded and an excellent example of impact-induced surface abrasion. (E) Lunar rock 14310 (approximately 20 cm long, 3439 g) shows a marked contrast between surfaces that were buried and those that were exposed to space. (F) Part of House Rock, a large breccia boulder from Apollo 16, displaying differential erosion of individual clasts versus matrix [NASA photograph AS16-106-17415]. See text for additional details.

it relates not only to the survival times of rocks on planetary surfaces, but also to the collisional fragmentation of entire solar-system objects, notably of asteroids and smaller satellites. The disruption of solid objects by impact is an intensely complex process in detail, with both the momentum and energy of the impactor requiring consideration in quantitative assessments of specific cases (*e.g.*, Housen and Holsapple, 1990). As even an abridged summary is beyond the scope of this paper, we will refer here only to the kinetic energy of the impactor for the sake of brevity. While it is an oversimplification, it nevertheless is a convenient term to use in a conceptual description of impact into an individual rock target at the scales considered here.

As defined by Gault and Wedekind (1969), an object is deemed collisionally "destroyed" when the mass of the largest, intact fragment (m_f) is at most half the mass of the initial object (m_0). The energy associated with the condition of $m_f = 0.5\ m_0$ is considered the critical "rupture" energy (E_r). When the actual kinetic energy of the impactor is larger than E_r, the target will be ruptured more severely, and the largest fragment will become $\ll 0.5\ m_0$. Events less energetic than E_r will result in a cratering event on the target object. The closer the energy to E_r, the larger the crater and the more prominent its associated fracture system.

Those fractures ultimately will engulf the entire target object, thus leading to its destruction. Gault et al. (1970, unpublished; see Hörz et al., 1974), Hörz and Cintala (1985) and Cintala and Hörz (2008) demonstrated that the critical rupture energy can also be delivered by multiple impacts, each $\ll E_r$. They experimented with projectile energies of 0.1 and 0.05 E_r, showing that E_r can be acquired cumulatively. This significantly reduces the lifetimes of surface rocks relative to the single-impact case at $\geq E_r$, because impacts at $< E_r$ are so much more frequent than those $\geq E_r$.

With the exception of regolith breccias that formed essentially in situ by shock compaction, all returned Apollo rocks are either primary ejecta fragments from bedrock or collisionally produced rubble of surface boulders, yet no morphologic or morphometric criteria exist to distinguish between these two scenarios. Nevertheless, unambiguous evidence for collisional fragmentation does occur for some rocks that suffered energetic impacts with less than the critical rupture energy. Fig. 6A, for instance, reveals a substantial, penetrating fracture emanating from a large pit; a slightly more energetic impact would have dislodged perhaps 20–30% of this rock's mass. Similarly, rock 73155 (Fig. 6B) bears a large pit and a pronounced, radial fracture array associated with this impact; there also is a concentric fracture system that appears to extend into the rock's interior (Compare this photograph to Fig. 4C for an experimental analog of the radial fractures and Fig. 4D for the subsurface fracture system.). There is little doubt that a slightly more energetic impactor would have destroyed rock 73155 of Fig. 6B.

Additional examples of the collisional fragmentation process can be seen in lunar-surface images of boulders. Fig. 6C shows an Apollo 14 boulder that was split in half. Note the fairly rounded (because it was

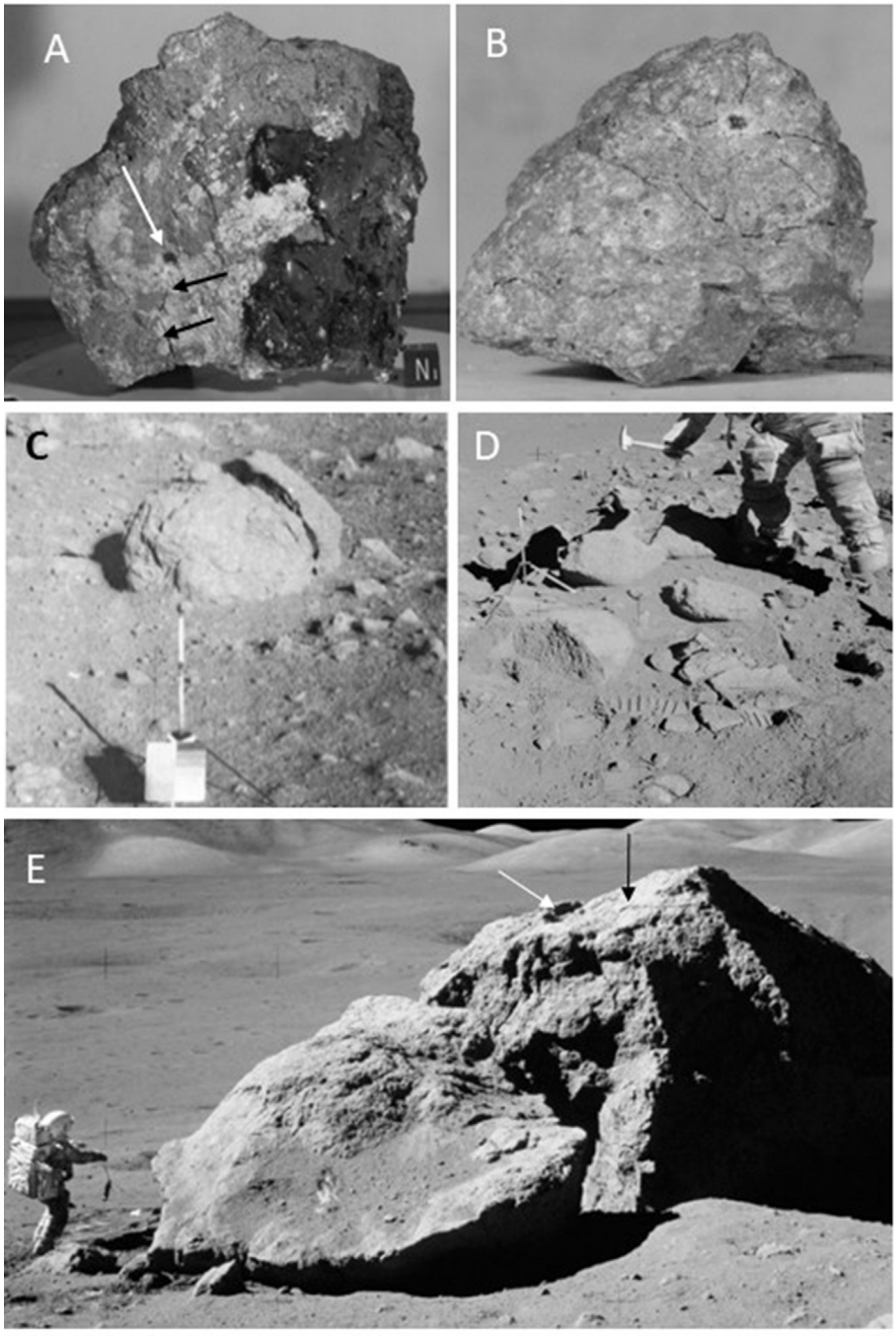

Fig. 6. Lunar examples of the collisional-fragmentation process. (A) Rock 64435 (1079 g; the cube is 1 cm on a side) suffered an energetic impact (white arrow) that produced a single penetrative fracture (black arrows). Note the highly eccentric spall zone relative to the glass-lined pit, caused by the removal of a local "promontory". [NASA photograph S72-39674]. (B) Crystalline impact melt 73155 (4 cm long, 79 g) suffered a near-catastrophic impact as evidenced by pronounced radial and concentric fractures [NASA photograph S73-17057]. (C) "Split Rock" (approximately 1 m in size) from Apollo 14 [NASA photograph AS14-68-9445]. (D) Surface scene from Apollo 15 site [NASA photograph AS15-82-11140]. (E) Large breccia boulder from Apollo 17 that was fractured into at least two major masses (see also Fig. 3D). Note the presence of an arc (white arrow), possibly reflecting a large spall of an impact centered on the black arrow. Note further the decimeter-scale fragments (close to the astronaut) that were dislodged from the boulder's daughter fragment [NASA photograph AS17-140-21496].

abraded) shape of this rock versus the sharp edges of the penetrative fracture, suggesting that the rupture event was fairly recent. A number of smaller rocks in the immediate vicinity of the split boulder are suggestive of fragments shed by the boulder prior to the splitting event. Fig. 6D illustrates relatively large fragments generated during the demise of a much larger parent at the Apollo 15 site.

Finally, Fig. 6E illustrates the most massive boulder visited by the Apollo 17 crew at the foot of the North Massif. The well-preserved regolith-track associated with this boulder rolling downhill indicates that the boulder was dislodged high up on the massif (Muehlberger et al., 1973). There is no bifurcation or any other evidence in this track that the boulder might have partly disintegrated during this downhill-tumbling episode, and the boulder must have come to rest at the end of its track as an intact object. We therefore suggest that the observed boulder split occurred after boulder emplacement, and that the breakup was due to a later impact. This view is supported also by the relatively jagged and fresh-appearing fracture surface, which contrasts with the more rounded and subdued surfaces of the parent boulder, thus suggesting a relatively recent event that split this boulder into two massive fragments. We also note that Ruesch et al. (2020) and Ruesch (2020) introduce additional examples of collisionally ruptured surface boulders based on Apollo and LROC photography.

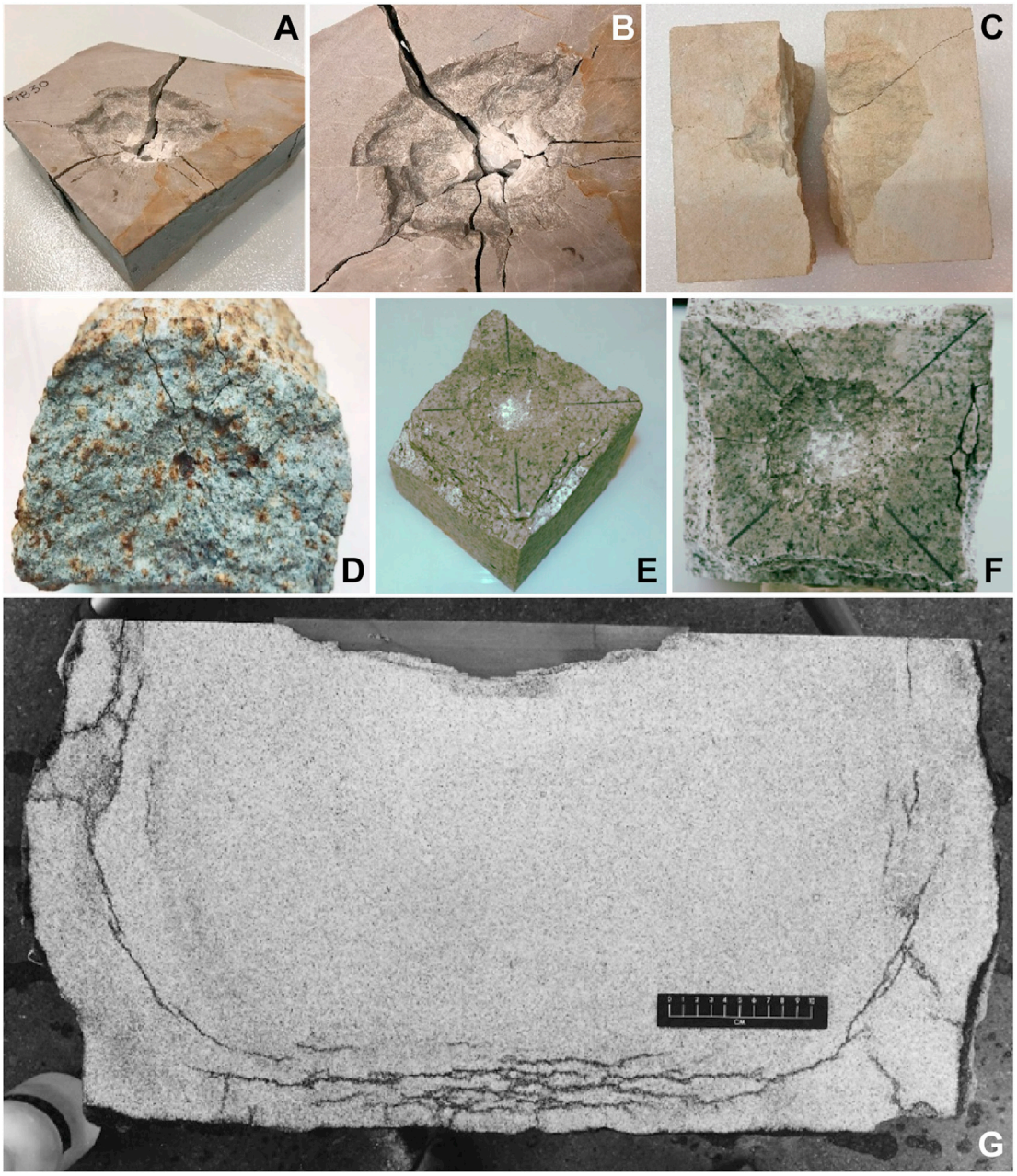

Fig. 7. Examples of laboratory experiments exploring the collisional fragmentation of rocks. (A) This 11-cm crater resulted from the impact of a 6.25-mm glass projectile at 2.3 km s^{-1} into an 8-cm thick slab of sandstone, 5.4 kg in mass. The impact actually disrupted the target into a few major fragments; the image shows the target after reconstruction (JSC EIL, unpublished). (B) Details of the crater in (A). (C) This limestone cube (approximately 20 x 20 × 15 cm, 12.8 kg) was split in half by an aluminum projectile at ~2.4 km s^{-1} (JSC EIL, unpublished). (D) Collisionally produced fragment (6 cm, 50 g) of an ordinary chondrite that developed radial fractures (Cintala and Hörz, 2008) associated with the impact of a 3.18-mm alumina sphere at 2.1 km s^{-1}. (E) and (F) Impact into a granodiorite cube (~10 cm on a side, 2.5 kg) by a 6-mm glass projectile at 2.2 km s^{-1}. (G) Cross section of the entire granite target (60 x 60 × 36 cm, 345 kg) accommodating the largest experimental crater in dense rock to date (1.25-cm aluminum sphere at 7.3 km s^{-1}; Hörz, 1969). This crater was also shown in Fig. 4C and D.

We now turn to laboratory impact experiments that explore the collisional fragmentation of finite-sized objects. Fig. 7A shows a block of sandstone that was used for a cratering experiment whose kinetic energy was large enough to generate deep fractures that are enlarged in Fig. 7B. Fig. 7C illustrates an impact into a limestone block at almost the ideal value of E_r, splitting the target into essentially equal halves. Note the size of the actual crater relative to the dimensions of this limestone target near the critical rupture energy, as well as the presence of additional, major fractures.

The results of a cratering experiment using an ordinary-chondrite target are shown in Fig. 7D, illustrating the generation of a radial fracture system surrounding the impact site. Note the difficulty in delineating the shallow, irregular spallation zone, even with relatively low-angle lighting. Fig. 7E and F shows a granodiorite cube, impacted by a glass sphere at approximately 0.3 E_r. These conditions were sufficient to induce substantial surface spallation on all four edges of the target face, leading to incipient rounding of the cube. Fig. 7F specifically is intended to show this rounding effect and that much more volume than that of the crater can be dislodged by spallation from the free surfaces of the target. Note that the edges of the cube bore the brunt of the spallation, as stress waves concentrate near such features (*e.g.*, Rinehart, 1975, pp. 178–179). These edges could be treated as the idealized equivalent of promontories that suffer spallation in natural rocks as described above.

Finally, Fig. 7G shows a cross section of the entire granite block and its crater that was already featured in Fig. 4C and D. Note that this large granite block was housed in a stout plywood box which was reinforced with steel bands; the space between the box and granite block was filled with high-strength urethane that was poured and foamed in place (Hörz, 1969). Without this confinement, most fractures in Fig. 7G would have resulted in complete spallation, again attesting to the ease with which large masses of rock — relative to crater volume — can be removed from a target's free surfaces. Spallation at free surfaces of a target, far removed from the actual crater cavity, will thus be an important contributor to the overall erosion as well as to the rounding (see Fig. 7E, F, and G) of surface rocks.

Experiments at $> E_r$ result in nondescript fragment populations and are not illustrated here. Note, however, that the most massive fragment even in these cases still bears some relation to the original target mass and impact energy in single-impact events that delivered as much as 100 E_r (*e.g.*, consult Fig. 18 in Hörz and Cintala, 1997).

It is also important to note that high-speed images of collisional fragmentation experiments have been used to determine the velocity distributions of the resulting fragments (*e.g.*, Nakamura et al., 1992). They show that the most massive fragments disperse at relatively modest speeds compared to the more fine-grained fractions. The finer fragments can disperse to large distances, commonly >10 times the parent boulder's diameter, thus most likely going unrecognized as the "siblings" of the larger pieces. Those larger pieces tend to cluster around the parent, commonly within 2–3 times the estimated diameter of the parent boulder. Fig. 6C, D, and E show such clustering of the more massive fragments. Obviously, when the impact energy is sufficient for the true annihilation of a rock (*e.g.*, >10 E_r), all fragments disperse at high speeds and most will probably not be associated spatially with the demise of a specific parent rock. It is thus possible that many collisional fragmentation events go unrecognized and that those that we can observe indeed represent relatively benign events, barely above E_r. This, in turn, is most likely accomplished by the cumulative effects of multiple impacts of modest energy as opposed to the single-impact case.

Ruesch (2020) and Ruesch et al. (2020) introduce examples of lunar-rock erosion that include the collisional fragmentation of boulders as well as the accumulation of abrasive debris on the sides of partly disaggregated parents. The net result is a mound-like structure composed of relatively large fragments and fine-grained material (*e.g.*, Fig. 3 of Reusch, 2020). Any local promontory will also act as a geometric shield for the ejecta from nearby regolith impacts, eventually to become a cone-shaped mound composed of fine-grained regolith only, at least at its surface (*e.g.*, Fig. 4 of Ruesch, 2020).

In summary, the collisional-fragmentation process is rather well understood experimentally. It is more efficient than abrasive impact processes in obliterating surface rocks. Examples of nearly catastrophic collisions can be observed in the Apollo rock collection, and examples of collisionally ruptured rocks exist in the Apollo surface images, ranging from rocks that are barely split to clusters of fragments that reflect the complete, in situ disintegration of a larger parent. Numerous, similar instances have been identified in Hayabusa images of the asteroid 25,143 Itokawa (Nakamura et al., 2008). It is also important to note, as illustrated by Fig. 5B and C, that the transition between impact-induced abrasion and collisional fragmentation processes is transitional. Many impacts can remove sizeable fractions of any target and/or produce penetrating fractures without "destroying" the rock as defined by the criterion of $m_f = 0.5\ m_0$. This merely serves to emphasize that a large fraction of rocks will be destroyed by the cumulative effects of multiple events having specific kinetic energies as small as 0.05 E_r (Hörz and Cintala, 1985), and possibly even smaller.

5. Rock erosion models and lunar surface observations

Cratering experiments using dense, crystalline rocks as targets establish the relationships between the kinetic energy and momentum of a projectile and the volume of the resulting crater, and thus of displaced crater mass. There is no subsurface movement in decimeter-sized, experimental craters in dense rocks, unlike the case for much larger, natural structures on the scale of kilometers and greater (*e.g.*, Croft, 1980; Melosh, 1989). The measured volume of an experimental crater in hard rock does indeed permit one to calculate the specific energy of cratering, *i.e.*, how much energy is needed to displace a unit mass of target. Typical experimental values for this specific cratering energy are in the range of 10^8 erg g^{-1} for crystalline rock (Gault et al., 1963; Gault, 1973; Holsapple and Schmidt, 1987). In contrast, experiments related to the collisional fragmentation of finite-sized, dense rocks show that the critical rupture energy necessary to displace half of the target is only in the range of 10^7 erg g^{-1} of initial target mass (Gault and Wedekind, 1969; Fujiwara et al., 1989; Housen and Holsapple, 1999; Cintala and Hörz, 2008). As previously discussed, collisional rupture is thus the much more efficient erosional process, essentially by an order of magnitude, compared to small-scale abrasion. The collisional process becomes more efficient because it allows for additional mass removal — beyond the displaced crater mass — by tensile failure at the free surfaces of finite-sized rocks, and because the generation and propagation of a few deep fractures consumes relatively little energy. Note, however, that these experimentally determined specific energies apply to laboratory-sized events only, with millimeter-scale impactors and centimeter to decimeter-sized craters.

A number of probabilistic models, based on Monte Carlo techniques, have simulated both particle abrasion and the collisional-fragmentation process, with the objective of arriving at absolute abrasion rates and collisional lifetimes of the hand-specimen sized rocks returned by Apollo. The discussions above indicate that the experimental inputs regarding specific energies for both processes seem to be well established, as is the size-frequency distribution of the impactors (*e.g.*, McDonnell et al., 1972; Neukum et al., 1973; Grün et al., 1985). The largest uncertainties relate to the actual flux of small scale (<1 cm) impactors on the lunar surface (*e.g.*, Fechtig et al., 1974; Grün et al., 1985, Love and Brownlee, 1993; Pokorny et al., 2019).

The abrasive erosion of lunar rocks was modeled by Ashworth and Mc Donnell (1973) and Hörz et al. (1974). Both arrived at a lunar erosion rate for hand-specimen sized rocks (<10 kg) on the order of 0.5–1mm/10^6 years. That rate, however, varies as a function of rock mass and will be less for much smaller objects and much higher for meter-sized, massive boulders. Obviously, physical properties, such as compressive and tensile strength, play a role as well. The calculated rate applies to dense, competent, and presumably typical basalt of 0.3 GPa

compressive strength (Gault et al., 1963).

If exposed to space, each lunar rock will suffer the effects of solar and high-energy cosmic radiation; these effects can be measured and related to total exposure time, such as the density of solar-flare tracks (Crozaz et al., 1974) or the abundances of cosmic-ray produced radionuclides such as ^{10}Be, ^{25}Al, ^{36}Cl, or ^{56}Co (Kohl et al., 1978). Depending on their respective energies, these charged particles will have characteristic penetration depths. In reality, measured depth profiles of tracks or radionmuclides deviate modestly from the ideal case because of the ongoing, continuous removal of surface material. This effect may then be used to derive actual rock-abrasion rates from these high-energy particle investigations. The latter are found to vary from 0.3 to 2 mm/10^6 years for individual rocks. The spread in rates is most likely due to the different physical properties of each specific rock analyzed. The majority of *observed* erosion rates based on solar-flare tracks, however, are in the range 0.5–1 mm/10^6 years (Crozaz et al., 1974). There is thus good agreement between three completely independent methods: impact modeling, solar-flare tracks, and radionuclides. We take this to imply that the major parameters and assumptions that are the foundations of the impact calculations are substantially correct, such as the energy distribution of the impactor population, as well as the actual energy flux.

We now address the survival times of rocks against collisional fragmentation as modeled by Hörz et al. (1975), using the assumptions about the total energy flux from the abrasion calculations described above. The rocks were modeled as cubes that had a compressive strength of 0.3 GPa, typical for basalt (Gault et al., 1963). Impacts as small as 0.1 E_r were allowed to contribute to the process. The major results of these calculations are illustrated in Fig. 8 and refer to rocks from 10 g to 10 kg in mass.

The 50% line in Fig. 8 is synonymous with the median survival time of rocks: half the number of rocks will have been destroyed and the other half remains after some specific time. We equate this time with "unit" time. Fig. 8 shows that *the destruction rate of rocks is not linear with time, regardless of rock mass*. The stochastic nature of the impact process leads to rather efficient rock destruction in the early stages of bombardment, as long as rocks occupy a sizeable fraction of the modeled surface. It also leaves a relatively long-lasting trail of "survivors," however, as the fraction of the surface that they occupy becomes small, and the probability of being targeted by sufficiently energetic impactors decreases. Note that it takes approximately 2.5 times longer than the unit time to destroy 90% of the modeled rock population and a factor of 3.5 longer to destroy 99%. The destruction of the "surviving" half (after unit time) of all original rocks will thus take a factor of 3–4 longer than it took to destroy the first half of all rocks. Also note that the last stragglers (>99%) can survive more than five times longer than the unit time. The important point is that the stochastic nature of the impact process produces nonlinear destruction rates with time and allows stragglers to reside at the surface longer than five times their nominal mean-survival time.

The model by Hörz et al. (1975) assumes identical physical properties for all rocks and consequently results in a linear relationship between absolute survival time and rock mass. This assumption must be updated on the basis of the work of Grady and Kipp (1980) and Housen and Holsapple (1999) who show that smaller objects are effectively stronger and require a larger E_r than larger ones, due to the existence and distribution of microscopic and eventually macroscopic flaws in almost all solids. Obviously, compressive strength and associated E_r are also highly variable for the suite of returned Apollo rocks. Fig. 8 specifically models rocks with basalt-like strengths. Despite all of these complications, not a single, measured exposure age for lunar rocks is longer than predicted from Fig. 8, as summarized in Figs. 12 and 13 of Hörz et al. (1975). Also, Fig. 2 in Hörz et al. (1975) depicts the largest craters observed on a number of Apollo rocks; none of those craters is larger than one would predict from an impact at 1 E_r, given the mass of its host rock. Thus, measured rock-exposure ages and the largest craters found on many Apollo rocks both suggest that the collisional-fragmentation calculations of Hörz et al. (1975) are in the appropriate range for rocks in the 0.001–10 kg mass range.

We now turn to observations at the lunar surface that address the survival times of large, meter-scale boulders. Numerous studies describe the morphologic degradation of "large" lunar craters with time. In this context, "morphologic degradation" refers to the gradual disappearance

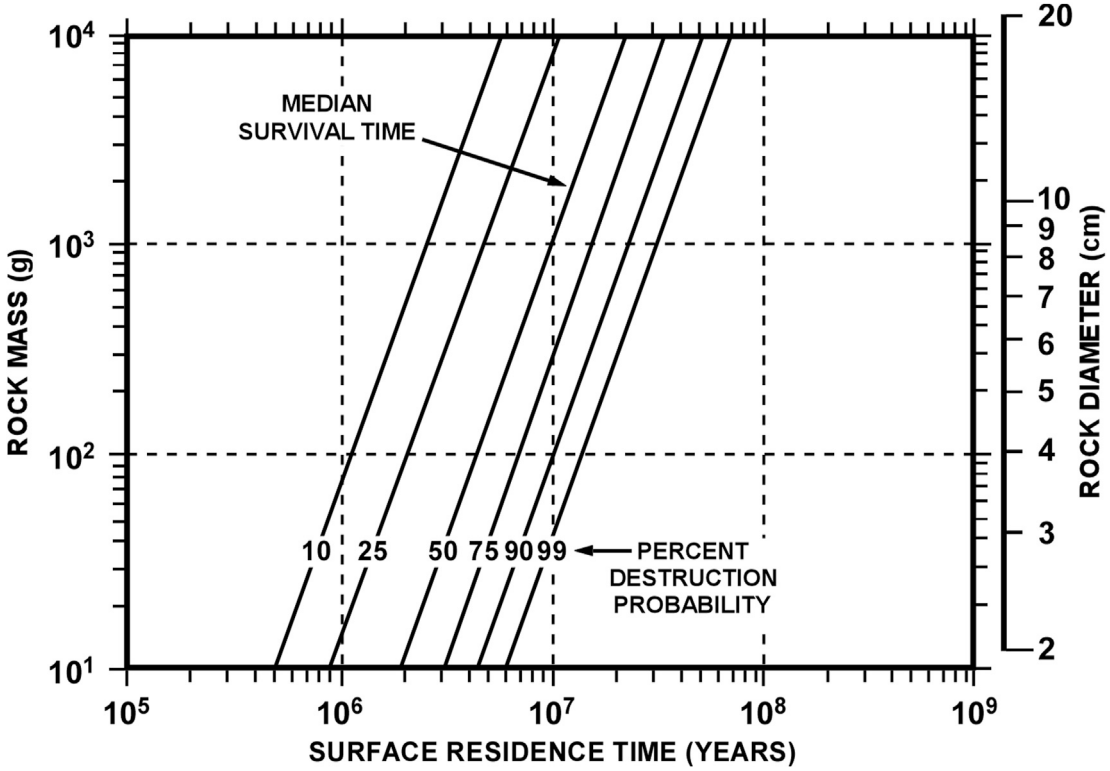

Fig. 8. Results of a Monte Carlo model, illustrating the absolute survival times of lunar rocks in the range 10 g to 10 kg in mass (Hörz et al., 1975). For details see text.

of an initially distinct, lobate, often striated, and boulder-strewn ejecta deposit, as well as to the gradual lowering of a crater's raised rim and the progressive infilling of the actual crater cavity. Basilevsky (1976) specifically addressed this morphologic degradation for craters smaller than a kilometer in diameter, ranking them in terms of degradational state and thus relative age. The Apollo landing sites contained such craters and a number of rocks were returned from their rims and ejecta deposits. The exposure ages of these rocks cluster around very specific values, which are then taken to date the actual formation age(s) of these modest-size craters, such as Cone Crater (26 Ma; Turner et al., 1971) at Apollo 14, South Ray Crater (2 Ma; *e.g.*, Behrmann et al., 1973) and North Ray Crater (50 Ma; Behrmann et al., 1973; Marti et al., 1973) at Apollo 16, and Camelot Crater (100 Ma) at Apollo 17. Combining these crater-formation ages with the craters' degradational stages has thus led to an understanding of the absolute timescales involved in the degradation of craters 0.1–1.0 km in diameter.

Using this Apollo-based "calibration" of crater degradation, Basilevsky et al. (2013) employed high-resolution images from the Lunar Reconnaissance Orbiter Camera (LROC) to analyze the frequency of meter-scale boulders in the ejecta deposits of these dated Apollo craters, as well as from a few other craters that were of intermediate or more advanced degradational state and relative age based on Basilevsky (1976). The number density (number per unit surface area) of boulders >2 m observed in the ejecta deposits of these craters correlates well with absolute crater-formation age(s) as illustrated in Fig. 9. Approximately half of meter-sized lunar surface boulders are destroyed after 50 Ma and few are left after about 200 Ma, consistent with the time-variable destruction rates discussed above. The observed median survival time at approximately 50 Ma is shorter, by approximately a factor of three, than one would extrapolate from Fig. 8 for specimens >1000 kg. We attribute this difference to two effects: (1) As mentioned above, scaled strength effects (Grady and Kipp, 1980; Housen and Holsapple, 1999 [see their Fig. 12]) entail that meter-scale boulders are effectively weaker than the <10 kg samples of Fig. 8; and (2) Hörz et al. (1974) integrated only over events >0.1 E_r, yet later experiments suggest that events as small as 0.05 E_r, if not still smaller, will contribute to weakening and disruption (Hörz and Cintala, 1985). Both effects would decrease the extrapolated model times and would bring them much closer to the actual lunar-surface observations of Basilevsky et al. (2013, 2015).

Yet another independent approach regarding the survival of boulders exposed at the lunar surface was explored by Gent et al. (2014), who used thermal-inertia measurements from the Diviner thermal radiometer aboard the Lunar Reconnaissance Orbiter (Paige et al., 2010). Blocky surfaces at the scale of meters retain heat longer than fine-grained regolith. Gent et al. investigated the ejecta deposits of craters with diameters of ~20–100 km and distinctly different degradational stages that could be ranked confidently into relative- and absolute-age progressions on the basis of crater-counting methods (*e.g.*, Hiesinger et al., 2012). Gent et al. demonstrated that the blockiness of the ejecta deposits correlated very well with crater age and the abundance of meter-scale boulders decreased beyond the detection limit of Diviner after approximately 10^9 years. Consistent with the earlier studies, Gent et al. found that the blocks disappear relatively rapidly during early periods of bombardment and tail out progressively with increasing residence time at the surface. In a subsequent paper, Gent et al. (2016) combined both Diviner data as well as radar observations from the LRO Miniature Radio Frequency instrument (Nozette et al., 2010), with the Mini-RF addressing the blockiness of the lunar subsurface to depths of a few meters. Significantly, smaller than those studied in their previous work (Gent et al., 2014), the craters investigated by Gent et al. (2016) were 10–15 km in diameter; they were also ranked by degradational stage and thus by relative and absolute age. This later study found that the population of surface rocks becomes totally depleted over time, but that the population of subsurface boulders remains substantially unchanged. This observation provides new and powerful constraints on the dynamic evolution and gardening rates of the lunar regolith.

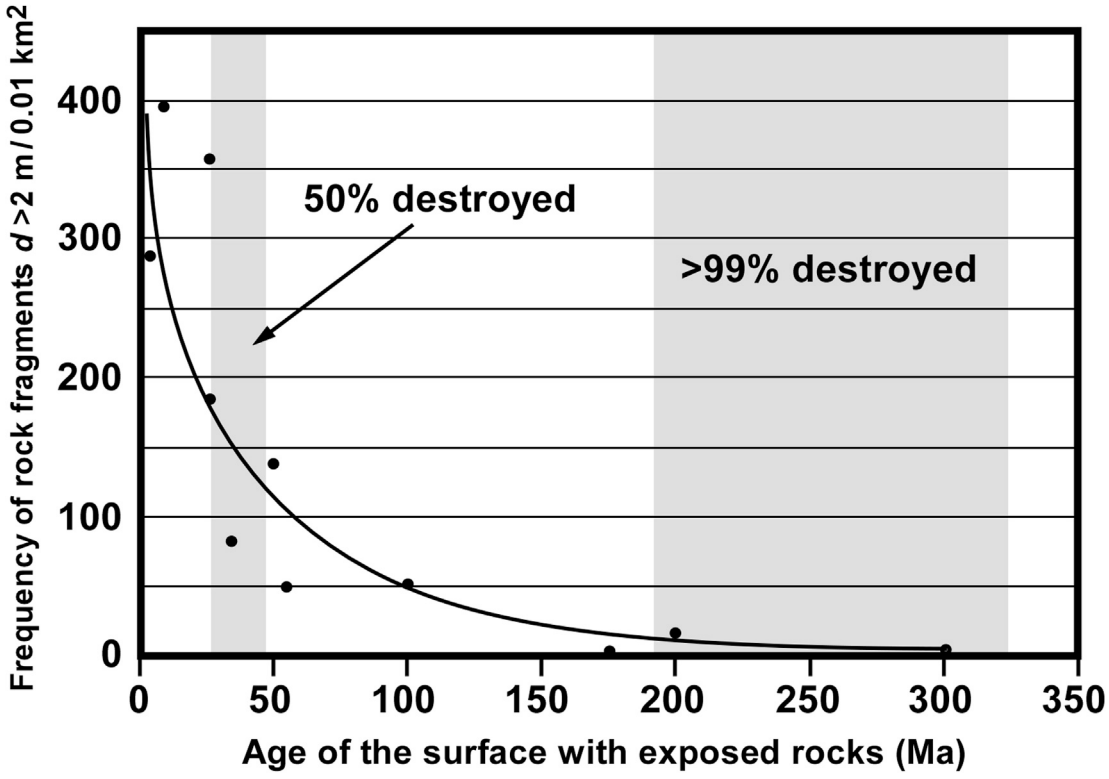

Fig. 9. Observationally determined survival times of lunar surface boulders >2m in size (Basilevsky et al., 2015). For details see text.

6. Generation of fine-grained regoliths

The ultimate and final product of the impact-triggered erosion process is the generation of a fine-grained regolith matrix. The components with sizes <1 cm totally dominate the loose regolith samples returned by Apollo. By convention, lunar "soils" are <1 mm in size; their average grain size by weight is generally in the range of 75–100 μm, with the <20 μm fraction commonly around 10% by weight (McKay et al., 1991). These are exceptionally fine-grained materials, and enormous amounts of energy are needed to produce them from relatively coarse rubble.

A wide range of evidence suggests that impact is the major process in generating this fine-grained material, foremost among which is the presence of impact-produced glasses. These glasses occur in two forms, the first of which is relatively transparent, mostly spherical, glass beads, the compositions of which cluster about that of local bedrock. They represent impact melts from local rocks, either from craters sufficiently large to penetrate the regolith and produce bedrock melts or from microcratering on surface rocks and boulders (Hörz and Cintala, 1997). Agglutinates, which are relatively opaque, clast laden, irregularly shaped to ropy melt particles, compose the second type of glass. They cluster around the average composition of the local soil (McKay et al., 1991), which is an intimate mixture of all local rocks and ballistically transported exotic components. The concentration of the transparent melt beads is typically a few percent by weight, but that of the agglutinates can be >50% of an entire lunar soil (McKay et al., 1991), attesting to the incessant processing and gardening of the regolith by small scale impacts (*e.g.* Costello et al., 2018).

The agglutinate melts characteristically contain numerous submicrometer-sized, paramagnetic spherules of metallic iron derived from Fe^{2+} in mafic minerals. Reduction of Fe^{2+} to metal occurs through the high temperatures generated by hypervelocity impact, possibly augmented by the presence of solar-wind implanted hydrogen in lunar-surface materials (Morris, 1976). Interestingly, the total concentration of agglutinates and that of the metallic blebs correlate with the absolute exposure times of soils. This provides a means of determining their production rates and — by proxy, since they are the dominant soil components — the impact-driven evolution and "maturation" of an entire soil sample (Morris, 1976; Heiken et al., 1991; McKay et al., 1991).

Note that the bulk compositions of individual sieve fractions of lunar soils vary, especially the <20-μm fraction, which is enriched in feldspathic components (Papike et al., 1982). By repeatedly impacting (up to 200 times) a rubbly gabbro target or others composed of either fragmented feldspar, pyroxene, or dunite, it was demonstrated experimentally that the dynamic comminution of rocks by shock waves is a mineral-specific process, with feldspar comminuting with greater ease than pyroxene or olivine (Hörz et al., 1984; Cintala and Hörz, 1992). Additionally, Papike et al. (1981, 1982) observed that the detailed composition of agglutinates is also somewhat enriched in the feldspathic soil component. They proposed that these melts are largely produced from the feldspar-enriched, finest fractions of the soil, a proposal that was substantiated via shock-recovery experiments at stresses of 32–78 GPa (Simon et al., 1985).

Finally, the complex process of "space weathering" — the modification of the surfaces of individual regolith grains at submicrometer scales — also involves a significant, impact-related component that operates in parallel with energetic solar and galactic particles (Keller and McKay, 1992; Noble et al., 2013; Pieters and Noble, 2016). These high-energy particles irradiate and sputter-erode materials exposed at the surface. As has been shown, impact erodes as well, but it also tends to deposit material, either as tiny melt splashes or as vapor deposits, at scales down to nanometers. The relative significance of impact versus radiation processes in generating and modifying these complex, multistage, surface materials is the subject of current debate and intensive research, but there is little doubt that impact-triggered melts and vapors are major contributors to space weathering on the Moon.

7. Discussion

7.1. 7a. Erosion by impact

This report attempts to summarize how the impact process erodes and comminutes rocks on the lunar surface, and it develops criteria by which the impact process might be distinguished from other erosive agents, such as thermal fatigue.

We described the detailed morphology of impact craters in solid rock. Craters <1 μm are composed of a glass-lined "pit" only, while craters >10 μm possess a prominent spall zone that surrounds the central pit; craters between 1 and 10 μm are transitional between those morphologies. Additionally, the pit resides in a high albedo "halo" of finely crushed and shocked material. In many cases, even fresh-appearing craters, the central pit has been lost, and all that remains is a finely crushed, high-albedo center and a spall zone. We suggest that removal of the pit becomes increasingly more prominent as crater size increases, and ultimately all craters in the decimeter-size range and larger will lose their pits as an integral part of the cratering process. Such "large" impact features will display only a relatively flat spall zone (or its eroded remnants), with a high-albedo patch in its center. At all scales, however, every impact leaves a circular depression that could still be recognizable in significantly eroded structures, in which both pit and high-albedo material are gone and the spall zone is preserved only in partial arcs. It is this centrosymmetric aspect of the mass-removal process that distinguishes hypervelocity impact from all other erosive mechanisms. Deviation from this symmetry is permitted for highly oblique impacts (Melosh, 1989) and in targets that are either physically heterogeneous at the scale of the evolving crater, including a substantial surface relief.

We also describe how bulk erosion of lunar-surface rocks and boulders occurs by processes of both impact abrasion and collisional fragmentation. Given the size frequency distribution of impact craters and its associated projectile-size distribution, abrasion reflects the low-energy "background" as opposed to the more efficient but much less frequent disruptive event(s). What constitutes the low-energy background versus a catastrophic event is very much a function of target mass, as the fate of a 1 kg rock versus a 10 ton boulder (equivalent to cubes with edges of ~7 cm vs. ~150 cm), for example, is obviously controlled by impact events of dramatically different energies and frequencies of occurrence. It follows that "large" boulders will have higher absolute abrasion rates than "small" rocks. By the same token, "small" rocks will have relatively short survival times because "energetic" impactors for small specimens are so much more frequent than they are for massive boulders. In the final analysis, collisional fragmentation dominates at all sizes, comminuting and eroding approximately *an order of magnitude more material* than abrasive mechanisms.

The abrasive impact process is not readily demonstrable with planetary-surface images, other than by the rounding of initially irregular and jagged shapes or surfaces. This rounding includes large boulders, with breccias frequently displaying rather knobby surface textures, if not outright protrusions, that reflect the different physical properties of component clasts and matrix. Rounding and differential erosion controlled by the physical properties of diverse rock components, however, might also be accomplished by other erosional processes and thus do not appear to be diagnostic of impact.

We suggest, however, that the collisional fragmentation process might be recognized in planetary surface images by a number of diagnostic criteria. "Split boulders" (see Fig. 6C and E), created by cracks that rupture a boulder in two (or into a few, large pieces) seem to be a telltale sign of impact. Also, the formation of radial and/or concentric fracture systems (*e.g.*, Fig. 6B or 7C) is diagnostic, especially for rocks that suffered impacts close to E_r and are near complete rupture. Collisionally fragmented rocks result in fragment clusters characterized by separation distances that mandate some horizontal acceleration of individual fragments. The Apollo 17 boulder and its fragments in Fig. 6E serve as an example, specifically the small fragments close to the astronaut. Note the

distance to their large parent. The same scene is viewed from a different angle in Fig. 3D, showing additional fragments. Also note the separation distances between the fragments shown in Fig. 6D. Such loose or "extended" clusters result from the kinetic energy remaining in each individual fragment upon catastrophic failure. As discussed above, high-speed imaging of experimental fragmentation events demonstrates that they are capable of accelerating and laterally displacing massive fragments over large distances (Nakamura et al., 1992). It is doubtful that any other process is capable of providing this lateral acceleration for such large and massive fragments. Most other erosional processes will lead to much tighter fragment clusters, if not piles of fragments, reflecting gravity-dominated, in situ degradation.

We also introduced evidence from the analysis of lunar soils regarding the role of impact in generating the fine-grained matrix of the lunar regolith. Impact-produced glass beads and agglutinates commonly make up 50% or more of individual soil samples. The finest fraction (<20 μm) of most lunar soils is enriched in feldspar, a consequence of mineral-specific comminution that has been duplicated experimentally in the laboratory by impact. On still smaller scales, the surfaces of many lunar grains display evidence for space weathering in the form of impact-generated melt splashes or vapor deposits. Impact also produces metallic-Fe beads over a wide range of sizes by reducing oxidized iron from mafic minerals at the high temperatures generated by shock heating at cosmic impact speeds. The study of lunar soils thus provides overwhelming evidence that impact is the dominant process on the Moon in accomplishing the erosion and comminution of surface rocks. Indeed, the final product of this process, the exceptionally fine-grained lunar soil, bears little mineralogical resemblance to the initial bedrock, because much of it has undergone melting and conversion into mineral detritus and polymict breccias. All of these modifications are driven by impact; most have been duplicated in the laboratory and are thus relatively well-understood.

In summary, on the basis of many observations of returned lunar samples, from images acquired at the surface or from orbit, from controlled laboratory experiments, and through some statistical modeling, one can derive an internally consistent view that impact is the dominant process of rock fragmentation and regolith formation on the Moon.

Throughout this report we mention and illustrate (*e.g.*, Figs. 3A, 5B and 5C, and 6A) the presence of impact-melt splashes on lunar rocks and the presence of centimeter-sized glass beads (*e.g.* Fig. 5B). Numerous additional examples could be given. Most of these glass surfaces are rather shiny, yet some are dull, depending on whether they are holohyaline or crystallized (See et al., 1986). No such melt splashes could be found in any photographs of Apollo boulders, despite detailed searches (Hörz, unpublished). On the other hand, the astronauts had little trouble recognizing and collecting such specimens as "unusual" surface rocks, with the majority collected in the vicinity of the young South Ray Crater on Apollo 16 (See et al., 1986). Such melt drapings represent an independent indicator of impact and might be encountered in the general surface imagery of other planetary surfaces.

7.2. 7b. Implications for thermal fatigue

We now turn to thermal fatigue as a potential agent in eroding and comminuting lunar surface rocks, and especially those on asteroids where thermal cycling appears to be more severe (Molaro and Byrne, 2012; Delbo et al., 2014; Molaro et al., 2017, 2019a,b; Lauretta et al., 2019). It is difficult to perform thermal-fatigue experiments because the thermal conductivity of rock is so low. The penetration of a thermal pulse to a suitable distance into a sample requires time; that time then determines the length of the heat-cool cycle. The deeper the desired penetration depth, the longer the required cycle and, with a realistic experiment taking thousands if not millions of such cycles, the experiment quickly becomes impractical. As a consequence, discussion of the process remains substantially theoretical by necessity, relating the heat-induced stress patterns and gradients to the orientation and distribution of overall strain and, ultimately, the generation and propagation of cracks and fracture systems. Some of the strain is parallel to the surface and may lead to exfoliation. For example, Lamp et al. (2017) used in situ field measurements, laboratory analyses, and numerical modeling to test the potential effects of thermal-stress weathering in the flaking of millimeter-thick alteration rinds seen on cobbles and boulders of dolerites in the Antarctic Dry Valleys. They found that during summer months, low-magnitude stresses due to temperature variations over time resulted in thermal-fatigue weathering, producing slow propagation of existing cracks, leading ultimately to flake detachment. This crack propagation appears to be facilitated through a reduction of fracture toughness.

Thermal fatigue seems capable of producing stresses high enough to split rocks in half (Molaro et al., 2017), thus leading to products that are similar to the collisional fragmentation outcomes shown in Figs. 6 and 7. The dominant expression of thermal fatigue, however, are stresses and cracks parallel to the illuminated surface, resulting in some form of exfoliation and the production of slab-like fragments. We have demonstrated that this is also a common form of impact-generated fragments (*e.g.*, spall plates from the zone surrounding the impact point) and do not consider slab-like fragments to be unique to either process. Indeed, the shapes of collisionally produced fragments can vary enormously, with rock texture and the specific energy of the impactor being major controlling factors. Given such a great variation, the shapes of impact-produced fragments will almost certainly overlap those produced by thermal fatigue. We thus suggest that fragment shape is not a good criterion for distinguishing between the two processes.

The acceleration of collisional fragments into "extended" clusters is not duplicated by thermal fatigue, as there will not be enough kinetic energy from thermally driven fragmentation to displace individual, massive fragments over sizeable distances, measured in multiples of the host rock diameter. Fragments resulting from thermal fatigue should be piled up rather close to their source, as local gravity only will act on them. For example, the "puzzle rocks" observed in the Antarctic Dry Valleys and attributed to thermal stresses (for example, Fig. 10 of Marchant and Head, 2007) are composed of multiple, closely spaced fragments that can readily be reassembled due to their lack of energetic displacement or rotation.

In its most general form, the centrosymmetric propagation of an impact-induced shock wave results in stress and strain distributions that differ dramatically from those imparted by thermal fatigue. These differences occur not only in overall geometry, but also in amplitude and strain rate by orders of magnitude. Centrally symmetric deformation features on planetary rock surfaces are thus the most telling evidence for impact. As illustrated by the lunar-rock collection, most impact features on rocks display circular spall zones or remnants thereof, and rare rocks display radial fracture systems, with or without a glass lined pit in their centers. Thermal fatigue lacks this centrosymmetric property.

Another potentially telling aspect for distinguishing between impact and thermal fatigue relates to current models of rock survival times as detailed in Hörz et al. (1975) and Delbo et al. (2014). As synthesized in Fig. 1 of Delbo et al. (2014), the larger a rock, the longer its survival time against collisional destruction, yet the trend for thermal fatigue is essentially the opposite. "Large" rocks exposed at the surface are destroyed with greater efficiency and have shorter, absolute survival times than do small rocks in the thermal-fatigue scenario. Because a large rock will not equilibrate thermally as readily as a small one, the large rock will build up much higher stresses between its warm surface and cold interior than a small one. Large rocks are thus destroyed more efficiently in the thermal-fatigue scenario. As shown earlier, the independent observations of Basilevsky et al. (2013, 2015) and Gent et al. (2014, 2016) regarding the frequency and demise of lunar-surface boulders strongly support the notion that larger surface specimens survive longer than small ones. The observational evidence on the Moon is thus contrary to the size- or mass-dependent predictions of the thermal-fatigue process and supports the impact-erosion scenario.

The above observations include the presence of a few 'stragglers' that exist multiple times longer at the surface than their mean survival time (Basilevsky et al., 2013, 2015), an expected feature that results from the stochastic nature of the impact process. In contrast, the thermal-fatigue process is a thermal-equilibrium phenomenon that equally affects *all* local rocks of a given size and composition. One would therefore expect actual survival times to cluster rather closely around some mean value for any population of such rocks. No rock will be destroyed until some critical fracture is produced over some time interval and all rocks should approach the stage of failure after rather similar (if not identical) exposure times. As a consequence, the distribution curve for the survival times for any specific population of rocks should be strongly peaked and substantially Gaussian for the thermal-fatigue scenario, which is fundamentally different from the exponential curve of impact erosion.

8. Conclusions

Rocks exposed at the surfaces of atmosphereless planetary bodies erode by a number of processes, such as sputtering, impact, thermal fatigue, and possibly others. Hypervelocity impact is characterized by the production of a high-pressure shock wave that propagates quasi-spherically into the target; this stress wave deposits sufficient energy to vaporize, melt, and fracture parts of any target rock. The centrosymmetric geometry, the amplitude of the stress wave, and the associated strain rates are not duplicated by any other geologic process. In combination, these characteristics lead to centrosymmetric crater structures and associated fracture systems, spallation processes at the target's free surfaces, and a host of phase transformations of the target rock, ranging from plasmas, vapors, and melts to high-pressure minerals and solid-state deformations. Examples and effects of these phenomena can be found throughout the lunar regolith, an extraordinarily dynamic sediment Costello et al. (2018) with a highly complex evolution of its mineralogy, petrography, and composition. (Heiken et al., 1991).

On the basis of lunar-surface observations, returned Apollo samples, and laboratory experiments, we have attempted in this report to develop criteria by which we can recognize impact as a process that can erode surface rocks. We emphasize macroscopic criteria that can assist in the interpretation of planetary surface images, including:

1) generally centrosymmetric depressions caused by spallation processes, which might or might not include a central, glass-lined pit and a highly crushed and shocked, high-albedo zone surrounding the pit,
2) radial or concentric fracture systems,
3) prominent fracture systems at the free surfaces of target rocks,
4) surface rocks either split in half or into a small number of clustered fragments, and
5) the possible presence of impact melt splashes on exposed rocks.

In many cases it will be impractical to distinguish among different processes, as they can generate similar products. Such ambiguous factors are the detailed shapes of rock fragments, the gradual rounding of rocks exposed at the surface, and the differential erosion of matrix and clasts, resulting in knobby surfaces of breccia boulders.

Identification of specific erosional processes also strongly depends on the spatial resolution of remotely obtained imagery or other information from spacecraft targeted to diverse planetary objects. For example, the information gleaned about the impact process solely from the interpretation of Apollo surface photography is minor compared to that extracted from detailed analysis of returned rocks and soils. Similar analyses might be possible with very high-resolution and/or microscopic imagers and supporting analytic instrumentation on landed spacecraft. In the absence of landers with such capabilities, however, only sample-return missions could unequivocally reveal the significance of small-scale impacts in the erosion of surface rocks and the overall evolution of regoliths on the Moon and other airless bodies.

While we favor impact as the dominant macroscopic, erosive process on the Moon, we expect that thermal fatigue would also be a contributing factor, especially on asteroids. A major goal for the community going forward is to develop criteria by which we can recognize the effects of thermal fatigue and to compare these to the impact criteria that we have advanced in this analysis. It is also very possible that the two processes complement each other. For example, is thermal fatigue enhanced by operating on rocks that have impact-induced microcracks and/or fracture systems? Regions permanently shielded from sunlight at the poles of the Moon are essentially at constant, albeit low, temperatures (Williams et al., 2017). Investigation of boulders, rocks, and soils from such permanently shadowed regions — either remotely or in the terrestrial laboratory — will reveal the effects of impact only, as all processes related to thermal cycling should be absent. We look forward to these developments and their application to our understanding of regolith evolution in the Solar System.

Author statement

Re.who did what

This is a review article that is the outgrowth of earlier papers by this group of authors on the subject of impact erosion and rock survival times, the latter senior authored by A. Basilevsky, who was thus a natural to come along. The present paper was substantially written by Friedrich Horz and Mark Cintala, due to their experience with Apollo rocks and experimental craters in dense rocks. James Head contributed examples of terrestrial erosion by thermal fatigue. All 4 authors participated in the iteration of this paper.

Re.additional info

This review article was motivated by the ever increasing prominence of thermal fatigue-related proposals that presumably shaped the surfaces and their rocks of asteroids Bennu and Ryuga as revealed by the recent OSIRIS REX and Hyabusa 2 missions. The paper points out that the evidence used in support of thermal fatigue processes is compatible also with impact in many cases. There is obviously lots of overlap between the two processes, and we encourage our colleagues to develop a list of diagnostic criteria for thermal fatigue, as we have done here for impact.

Declaration of competing interest

The authors declare that they have no known competing financial interests or personal relationships that could have appeared to influence the work reported in this paper.

Acknowledgements

We appreciate the skill and dedication with which R. Montes, F. Cardenas, and the late G.L. Haynes conducted many experiments mentioned in this paper. Emily S, Costello and an anonymous reviewer provided helpful comments. All authors gratefully acknowledge their financial support from diverse sources: FH from JETS Contract Task "Planetary Process Simulation" at NASA Johnson Space Center (ES0379254100007), ATB from the Program of Support of the State Academies for 2013–2020 (State Assignment No. 0137–0001), JWH from the NASA Lunar Orbiter Lunar Orbiting Laser Altimeter Team (80NSSC19K0605), and MJC from NASA's Planetary Science Research Program.

Appendix A. Supplementary data

Supplementary data to this article can be found online at https://doi.org/10.1016/j.pss.2020.105105.

References

Ashworth, D.G., McDonnell, J.A.M., 1973. Lunar surface micr-erosion related to interplanetary dust particle distributions. Space Res. XIII 1071–1083.

Ballouz, R.L., the Osiris Rex Team, 2020. Mini-craters on (101955) Bennu's boulders: deriving the impact strength of C-type asteroids. In: Lunar and Planet. Sci. Conf. 51st. Abstract #2737.

Basilevsky, A.T., 1976. On the evolution of small lunar craters. In: Proc. Lunar Sci. Conf. 7th, pp. 1005–1020.

Basilevsky, A.T., Head, J.W., Hörz, F., 2013. Survival Times of meter-sized boulders on the surface of the Moon. Planet. Space Sci. 89, 118–126.

Basilevsky, A.T., Head, J.W., Hörz, F., Ramsey, K., 2015. Survival times of meter-sized boulders on the surface of airless bodies. Planet. Space Sci. 117, 312–328.

Behrmann, C., Crozaz, G., Drozd, R., Hohenberg, C., Ralston, C., Walker, R., Yuhas, D., 1973. Cosmic-ray exposure history of North Ray and South Ray material. In: Proc. Lunar Sci. Conf. 4th, pp. 1857–1874.

Cintala, M.J., Hörz, F., 2008. Experimental impacts into chondritic targets, part 1: disruption of an L6 chondrite by multiple impacts. Meteoritics Planet Sci. 43, 771–803.

Cintala, M.J., Hörz, F., 1992. An experimental evaluation of the mineral specific comminution. Meteoritics 27, 395–403.

Croft, S.K., 1980. Cratering flow fields: implications for the excavation and transient expansion stages of crater formation. In: Proc. Lunar and Planet. Sci. Conf. 11th, pp. 2347–2378.

Crozaz, G., Drozd, D., Hohenberg, C., Morgan, C., Ralston, C., Walker, R.M., Juhas, D., 1974. Lunar surface dynamics: some general conclusions and new results from Apollo 16 and 17. In: Proc. Lunar Sci. Conf. 5th, pp. 2475–2499.

Costello, E.S., Gent, R.R., Lucey, P.G., 2018. The mixing of the lunar regolith: viral updates to a canonical model. Icarus 314, 327–344.

Davis, D.R., Ryan, E.V., 1990. On collisional disruption: experimental results and scaling laws. Icarus 83, 156–182.

Delbo, M., Libourel, G., Murdoch, N., Michel, P., Ramesh, K.T., Ganino, C., Verati, C., Marchi, S., 2014. Thermal fatigue as the origin of regolith on small asteroids. Nature 508, 233–236.

Fechtig, H., Hartung, J.B., Nagel, K., Neukum, G., 1974. Lunar microcrater studies, derived meteor fluxes, and comparison with satellite-borne experiments. Proc. Lunar Sci. Conf. 5th. 2460–2474.

Flynn, G.J., Durda, D.D., 2004. Chemical and mineralogical size segregation in the impact disruption of inhomogeneous, anhydrous meteorites. Planet. Space Sci. 52, 1129–1140.

Fujiwara, A., Cerroni, P., Davis, D., Ryan, E., De Martino, M., Holsapple, K.A., Housen, K.R., 1989. Experiments and scaling laws for catastrophic collisions. In: Binzel, R.P., et al. (Eds.), Asteroids II. University of Arizona Press, Tucson, pp. 240–265.

Gault, D.E., Wedekind, J.A., 1969. The destructions of tektites by micrometeorite impact. J. Geophys. Res. 74, 6780–6794.

Gault, D.E., Shoemaker, E.M., Moore, H.J., 1963. Spray Ejected from the Lunar Surface by Meteoroid Impact. NASA TN D-1767.

Gault, D.E., 1973. Displaced mass, depth, diameter and effects of oblique trajectories for impact craters formed in dense crystalline rock. Moon 4, 32–44.

Gent, R.R., Hayne, P.O., Bandfield, J.L., Campbell, B.A., Allen, C.C., Carter, L.M., Paige, D.A., 2014. Constraints on the recent rate of lunar ejecta breakdown and implications for lunar crater ages. Geology 42, 1059–1062. https://doi.org/10.1130/G35926.1.

Gent, R.R., Carter, L.M., Bandfield, J.L., Udovicic, T., Campbell, B.A., 2016. Lunar crater ejecta: physical properties revealed by radar and thermal infrared observations. Icarus 273, 182–195. https://doi.org/10.1016/j.icarus.2015.12.014.

Grady, D.E., Kipp, M.E., 1980. Continuum modeling of explosive fracture in oil shale. Int. J. Rock Mech. Min. Sci. 17, 147–157.

Grün, E., Zook, H.A., Giese, R.H., 1985. Collisional balance of the meteoritic complex. Icarus 62, 244–272.

Hartmann, W.K., 1985. Impact experiments 1. Ejecta velocity distributions and related results from regolith targets. Icarus 63, 69–98.

Hartung, J.B., Hörz, F., Gault, D.E., 1972a. Lunar microcraters and interplanetary dust. In: Lunar Sci. Conf. 3rd, pp. 2735–2753.

Hartung, J.B., Hörz, F., McKay, D.S., Biamonte, F., 1972b. Surface features on glass spherules from the Luna 16 sample. Moon 5, 436–446.

Heiken, G.H., Vaniman, D., French, B.M. (Eds.), 1991. Lunar Sourcebook: A User's Guide to the Moon. Cambridge University Press, New York, p. 736.

Hiesinger, H., Bogert, C.H., Paschkert, J.H., Funcke, L., 2012. How old are young lunar craters? J. Geophys. Res. 117, E00h10. https://doi.org/10.1029/2011JE003935.

Holsapple, K.A., Schmidt, R.M., 1987. Point source solutions and coupling parameters in cratering mechanics. J. Geophys. Res. 92, 6350–6376.

Hörz, F., 1969. Structural and mineralogical evaluation of an experimentally produced impact crater in granite. Contrib. Mineral. Petrol. 21, 365–377.

Hörz, F., Hartung, J.B., Gault, D.E., 1971a. Micrometeorite craters on lunar rock surfaces. Earth Planet Sci. Lett. 10, 381–386.

Hörz, F., Hartung, J.B., Gault, D.E., 1971b. Micrometeorite craters on lunar rock surfaces. J. Geophys. Res. 89, C183–C196.

Hörz, F., Morrison, D.A., Hartung, J.B., 1972. The surface orientation of some Apollo 14 rocks. Mod. Geol. 3, 93–104.

Hörz, F., Schneider, E., Hill, R.E., 1974. Micrometeoroid abrasion of lunar rocks: a Monte Carlo simulation. In: Proc. Lunar Sci. Conf. 5th, pp. 2397–2412.

Hörz, F., Schneider, E., Gault, D.E., Hartung, J.B., Brownlee, D.E., 1975. Catastrophic rupture of lunar rocks: a Monte Carlo simulation. Moon 13, 235–258.

Hörz, F., Cintala, M.J., See, T.H., Cardenas, F., Thompson, T.D., 1984. Grain size evolution and fractionation trends in an experimental regolith. In: Proceedings of the 15th Lunar and Planetary Science Conference, in Journal of Geophysical Research, vol. 89, pp. C183–C196.

Hörz, F., Cintala, M.J., 1985. Collisional fragmentation of granodiorite targets by multiple impact events. In: Lunar Planet. Sci. Conf. 16th, pp. 404–406.

Hörz, F., Grieve, R.A.F., Heiken, G.H., Spudis, P., Binder, A., 1991. Lunar surface processes. In: Heiken, G.H., Vaniman, D., French, B.M. (Eds.), Lunar Sourcebook: A User's Guide to the Moon. Cambridge University Press, New York, pp. 73–120.

Hörz, F., Cintala, M.J., 1997. Impact experiments related to the evolution of planetary regoliths. Meteoritics Planet Sci. 32, 179–209.

Housen, K.R., Holsapple, K.A., 1990. On the fragmentation of asteroids and planetary satellites. Icarus 84, 226–253.

Housen, K.R., Holsapple, K.A., 1999. Scale effects in strength-dominated collisions of rocky asteroids. Icarus 142, 21–33.

Keller, L.P., McKay, D.S., 1992. Micrometer-sized glass spheres in Apollo 16 soil 61181: implications for impact volatilization and condensation. In: Proc. Lunar Planet. Sci. Conf. 22nd, pp. 137–144.

Kieffer, S.W., 1971. Shock metamorphism of the coconino sandstone at meteor crater, AZ. J. Geophys. Res. 76, 5449–5473.

Kohl, C.P., Murrell, M.T., Russ III, C.P., Arnold, J.R., 1978. Evidence for the constancy of the solar cosmic ray flux over the past ten million years: ^{53}Mn and ^{26}Al measurements. In: Proc. Lunar Planet. Sci. Conf. 9th, pp. 2299–2310.

Lamp, J.L., Marchant, D.R., Mackay, S.L., Head III, J.W., 2017. Thermal stress weathering and the spalling of Antarctic rocks. J. Geophys. Res. 121, 3–24. https://doi.org/10.1002/2016JF003992.

Lauretta, D.S., 45 co-authors, 2019. OSIRIS-REx arrives at asteroid (101955) Bennu: exploration of a hydrated primitive near-Earth asteroid. In: Lunar Planet. Sci. 50th. Abstract 2608.

Love, S.G., Brownlee, D.E., 1993. A direct measurement of the terrestrial mass accretion rate of cosmic dust. Science 262, 550–553.

Marchant, D.R., Head, J.W., 2007. Antarctic dry valleys: microclimate zonation, variable geomorphic processes, and implications for assessing climate change on Mars. Icarus 192, 187–222. https://doi.org/10.1016/j.icarus.2007.06.018.

Marti, K., Lightner, B.G., Osborne, T.W., 1973. Krypton and xenon in some lunar samples and the age of North Ray Crater. In: Proc. Lunar Sci. Conf. 4th, pp. 2017–2048.

McDonnell, J.A.M., Ashworth, D.G., Flavil, R.P., Jennison, R.C., 1972. Simulated microscale erosion on the lunar surface by hypervelocity impact, solar wind sputtering, and thermal cycling. In: Proc. Lunar Sci. Conf. 3rd, pp. 2755–2765.

McKay, D.S., Heiken, G.H., Basu, A., Blanford, G., Simon, S.B., Reedy, R., French, B.M., Papike, J.J., 1991. The lunar regolith. In: Heiken, G.H., Vaniman, D., French, B.M. (Eds.), Lunar Sourcebook: A User's Guide to the Moon. Cambridge University Press, New York, pp. 285–356.

Melosh, H.J., 1989. Impact Cratering: a Geologic Process. Oxford University Press, New York, p. 245.

Minton, D.A., Fassett, C.I., Hirabayashi, M., Howl, B.A., Richardson, J.E., 2019. The equilibrium size-frequency distribution of small craters reveals the effects of distal ejecta on lunar landscape morphology. Icarus 322. https://doi.org/10.1016/j.icarus.02.021.

Molaro, J.L., Byrne, S., 2012. Rates of temperature change on airless landscapes and implications for thermal stress weathering. J. Geophys. Res. 117, E10011. https://doi.org/10.1029/2012JE004138.

Molaro, J.L., Byrne, S., Lee, J.-L., 2017. Thermally induced stresses in boulders on airless body surfaces, and implications for rock breakdown. Icarus 294, 247–261.

Molaro, J.L., 12 co-authors, 2019a. Fracture Formation Mechanisms on Bennu and evidence of thermally driven breakdown. In: Lunar Planet. Sci. 50th. Abstract 1597.

Molaro, J.L., 12 co-authors, 2019b. Distribution of cracked boulders on (101955) Bennu: searching for evidence of solar-induced thermal stress. In: Lunar Planet. Sci. 50th. Abstract 1457.

Morris, R.V., 1976. Surface exposure indices of lunar soils: a comparative FMR study. In: Proc. Lunar Sci. Conf. 7th, pp. 315–335.

Morrison, D.A., McKay, D.S., Heiken, G.H., 1972. Microcraters on lunar rocks. In: Proc. Lunar Sci. Conf. 3rd, pp. 2767–2787.

Muehlberger, W.R., 19 co-authors, 1973. Preliminary Geologic Investigation of the Apollo 17 Landing Site. In: Apollo 17 Preliminary Science Report. NASA SP-330, Washington, DC, 6-1 - 6-91.

Nakamura, A.M., Suguiyama, K., Fujiwara, A., 1992. Velocity and spin of fragments from impact disruptions I. An experimental approach to a general law between mass and velocity. Icarus 100, 127–135.

Nakamura, A.M., Michikami, T., Hirata, N., Fujiwara, A., Nakamura, R., Ishiguro, M., Miyamoto, H., Demura, H., Hiraoka, K., Honda, T., Honda, C., Saito, J., Hashimoto, T., Kubota, T., 2008. Impact process of boulders on the surface of asteroid 25143 Itokawa — fragments from collisional disruption. Earth Planets Space 60, 7–12.

Neukum, G., Schneider, E., Mehl, A., Storzer, D., Wagner, G.A., Fechtig, H., Bloch, M.R., 1972. Lunar craters and exposure ages derived from crater studies and solar flare tracks. Lunar Sci. Conf. 3rd, 2793–2810.

Neukum, G., Hörz, F., Morrison, D.A., Hartung, J.B., 1973. Crater populations on lunar rocks. In: Proc. Lunar Sci. Conf. 4th, pp. 3255–3276.

Noble, S.K., Keller, L.P., Christofferson, R., Rhaman, Z., 2013. Lateral variations in lunar weathering patina on centimeter to nanometer scales. In: Lunar Planet. Sci. Conf. 44th. Abstract 1298.

Nozette, S., Spudis, P.D., Bussey, B.J., Jensen, R., Rainey, K., Winters, H., Lichtenberg, C.L., Marinelli, W., Crusan, J., Gates, M., Robinson, M.S., 2010. The lunar reconnaissance orbiter miniature Radio frequency (Mini-RF) technology demonstration. Space Sci. Rev. 150, 285–302.

Paige, D.A., 22 coauthors, 2010. The lunar reconnaissance orbiter diviner lunar radiometer experiment. Space Sci. Rev. 150, 125–160.
Papike, J.J., Simon, S.B., White, C., Laul, J.C., 1981. The relationship of the lunar regolith <10 μm fraction and agglutinates, Part I: a model for agglutinate formation and some indirect supportive evidence. In: Proc. Lunar Planet. Sci. Conf. 12th, pp. 409–420.
Papike, J.J., Simon, S.B., Laul, J.C., 1982. The lunar regolith: chemistry, mineralogy, and petrology. Rev. Geophys. Space Phys. 20, 761–826.
Pieters, C.M., Noble, S.K., 2016. Space weathering on airless bodies. J. Geophys. Res. – Planets. 121, 1865–1884.
Pokorny, P., Janches, D., Santos, M., Szalay, J.R., Horanyi, M., Nesvorny, D., Kuchner, M.J., 2019. Meteoroids at the Moon: orbital properties, surface vaporization, and impact ejecta production. J. Geophys. Res.– Planets. 124, 752–778.
Quaide, W.L., Oberbeck, V.R., 1975. Development of the mare regolith: some model considerations. Moon 13, 27–55.
Rinehart, J.S., 1975. Stress Transients in Solids. Hyperdynamics, Santa Fe, NM, p. 230.
Ruesch, O., 2020. Impacts without craters: in situ observations of fragmented blocks on the Moon. In: Lunar Planet. Sci. Conf. 51st. Abstract # 2118.
Ruesch, O., Sefton-Nash, E., Vago, J.L., Küppers, M., Pasckert, J.K., Khron, K., Otto, K., 2020. In situ fragmentation of lunar blocks and implications for impacts and solar-induced thermal stress. Icarus 336. https://doi.org/10.1016/j.icarus.2019.113431.
Ryan, E.V., Hartmann, W.K., Davis, D.R., 1991. Impact experiments 3: catastrophic fragmentation of aggregate targets and relation to asteroids. Icarus 94, 283–298.
See, T.H., Hörz, F., Morris, R.V., 1986. Apollo 16 impact melt splashes and major element composition. In: Proc. Lunar Planet Sci Conf 17th, in J.Geophys. Res, vol. 91, pp. E3–E20.
Schneider, E., Storzer, D., Hartung, J.B., Fechtig, H., Gentner, W., 1973. Microcraters on Apollo 15 and 16 samples and corresponding cosmic dust fluxes. In: Proc. Lunar Sci. Conf. 4th, pp. 3277–3290.
Simon, S.B., Papike, J.J., Hörz, F., See, T.H., 1985. An experimental investigation of agglutinate melting mechanisms: shocked mixtures of Apollo 11 and 16 soils. In: Proc. Lunar Planet. Sci. Conf. 17th, in J. Geophys. Res, vol. 90, pp. E64–E74.
Speyerer, E.J., Povilaitis, R.Z., Robinson, M., Thomas, P.T., Wagner, R.V., 2016. Quantifying crater production and regolith overturn on the Moon with temporal imaging. Nature 538, 215–218.
Turner, G., Huneke, J.C., Posodek, F.A., Wasserburg, G.J., 1971. ^{40}Ar-^{39}Ar and cosmic ray exposure ages of Apollo 14 samples. Earth Planet Sci. Lett. 12, 19–35.
Ulrich, G.E., Hodges, C.A., Muehlberger, W.R., 1981. Geology of the Apollo 16 Area, Central Lunar Highlands. U. S. Geol. Surv. Prof. Paper 1048.
Williams, J.P., Greenhagen, B., Soften-Nash, E., 2017. The global surface temperatures of the Moon as measured by the diviner lunar orbiter radiometer experiment. Icarus 283, 300–325.